npj | climate and atmospheric science

Article

Published in partnership with CECCR at King Abdulaziz University

https://doi.org/10.1038/s41612-026-01369-w

Highly light-absorbing particle emissions from low-sulfur marine fuels

Tuukka Kokkola[1] ✉, Timothy A. Sipkens[2], Andreas Paul[3,12], Deeksha Shukla[4,5], Mika Ihalainen[1], Anusmita Das[4,5], Jason Scott[2], Johannes Passig[4,5,6], Aleksandrs Kalamašņikovs[4,5,6], Uwe Etzien[7], Zheng Fang[8], Santtu Mikkonen[1], Anni Hartikainen[1], Viljami Luostari[1], Arya Mukherjee[1], Hendryk Czech[4,5], Martin Sklorz[4,5,6], Bert Buchholz[7], Thorsten Streibel[4,5], Thorsten Hohaus[3], Yinon Rudich[8], Johan Øvrevik[9,10], Ralf Zimmermann[1,4,5,6,11], Joel C. Corbin[2] & Olli Sippula[1,11] ✉

Particulate matter (PM) from marine traffic interacts with solar radiation and clouds, ultimately influencing Earth's radiative balance. Ships operated with conventional fossil fuel oils emit light-absorbing carbonaceous PM that offsets aerosol-driven cooling and can even exert a net positive radiative forcing, i.e. warming effect. Radiative properties of PM are possibly further altered by atmospheric aging processes, the effects of which are not fully understood. We present black carbon (BC) emission factors (EF) and optical properties of fresh and photochemically aged particle emissions from a marine engine, operated using low-sulfur heavy fuel oil (LS-HFO) and marine gas oil (MGO), complying with recent maritime sulfur regulations by the International Maritime Organization (IMO). The fresh particle emissions comprised mostly BC, with average BC EFs of 144 and 43.2 mg/kWh for LS-HFO and MGO, respectively. Light absorption was mostly attributed to BC in particles from both fuels, with absorption Ångström exponent (AAE, 370 to 880 nm) values 0.9–1.0 (interquartile range), and 870 nm single scattering albedo (SSA) values 0.15–0.24 during the full cycles. Fresh LS-HFO emissions exhibited lower SSA values than those of high-sulfur fuels reported in literature, primarily associated with reduced sulfate emissions. Photochemical aging led to an absorption enhancement (E_{abs}) of 1.2–1.5 and an increase in SSA relative to fresh emissions, although SSA remained below 0.5, and the estimated direct radiative forcing effect stayed positive. Our results show that sulfur-compliant marine fuels can emit highly absorbing particles with an atmospheric warming potential, which is mostly maintained even after photochemical aging.

Environmental and health concerns around sulfur air pollution from ship emissions have led to stricter limits on sulfur content in marine fuels. In 2015, the International Maritime Organization (IMO) implemented a fuel sulfur content (FSC) limit of 0.1% for Sulfur Emission Control Areas (SECA)[1], including the Baltic and North Sea, North America, and the Caribbean Sea. The Mediterranean Sea was later appended to SECAs in 2025. In 2020, the IMO set a global FSC limit of 0.5%, which has effectively prohibited the use of conventional heavy fuel oil (HFO) with a high sulfur content, or requires the use of a sulfur scrubber for non-compliant fuels[2,3]. Instead of completely transitioning to cleaner fuels alongside recent global sulfur regulations, the marine sector implemented low-sulfur variants of residual fuels (e.g., low-sulfur heavy fuel oil [LS-HFO], very-low sulfur fuel

---

[1]Department of Environmental and Biological Sciences, University of Eastern Finland, Kuopio, Finland. [2]Metrology Research Centre, National Research Council Canada, Ottawa, ON, Canada. [3]Institute of Climate and Energy Systems: Troposphere (ICE-3), Forschungszentrum Juelich, Juelich, Germany. [4]Chair of Analytical Chemistry, Institute of Chemistry, University of Rostock, Rostock, Germany. [5]Cooperation Group "Comprehensive Molecular Analytics", Helmholtz Zentrum München, Neuherberg, Germany. [6]Department Life, Light and Matter (LL&M), University of Rostock, Rostock, Germany. [7]Chair of Piston Machines and Internal Combustion Engines (LKV), Faculty of Mechanical Engineering and Marine Technology, University of Rostock, Rostock, Germany. [8]Department of Earth and Planetary Sciences, Weizmann Institute of Science, Rehovot, Israel. [9]Division of Climate and Environmental Health, Norwegian Institute of Public Health, Oslo, Norway. [10]Department of Biosciences, University of Oslo, Oslo, Norway. [11]Department of Chemistry, University of Eastern Finland, Joensuu, Finland. [12]Present address: Department of Chemistry, Aarhus University, Aarhus, Denmark. ✉e-mail: tuukka.kokkola@uef.fi; olli.sippula@uef.fi

oil [VLSFO], and ultra-low sulfur fuel oil [ULSFO]) to comply with the limit while maintaining the economic advantages of using HFO. A recent advancement in phasing out highly polluting residual fuels was the ban on the use and transport of HFO in Arctic regions, which started in July 2024 and will be fully in force by July 2029[4]. This is an important step forward, as HFO poses substantial risks to the Arctic environment, while disproportionate warming of the Arctic has seen the extent of Arctic sea ice declining year-by-year[5–7], with similar trends observed in adjacent regions such as the Baltic sea[8]. This decline in Arctic sea ice is projected to open new potential routes for intercontinental marine transportation, extend navigability for existing routes, and increase accessibility to Arctic ports[9]. Arctic shipping has increased by 37% between 2013 and 2023[10] and is likely to continue rising as the rapid retreat of Arctic sea ice expands navigability in the area.

Current forms of shipping emit high quantities of particulate matter (PM), which are classified as short-lived climate forcers (SLCF). Historically, much of the aerosols emitted by marine vessels have contributed to atmospheric cooling by scattering solar radiation and increasing cloud seeding and brightness over oceans[11]. However, sulfate aerosol emissions, which are light-scattering and effective cloud condensation nuclei by nature, have substantially decreased after the enforcement of the IMO 2020 sulfur regulations. The reduction of the sulfate-driven cooling effect from ship emissions has been projected to exert a net warming effect[12–15], but it remains under investigation if it is already connected to the recent sea surface temperature anomalies in the Northern Hemisphere[14]. While the projected warming effect is generally agreed upon, the extent of warming for the coming decades remains uncertain. For example, the effective radiative forcing (ERF) following global sulfur regulations has been estimated at approximately +0.12[14] or +0.13[13] W/m^2, but published values span a range from +0.02[16] to +0.33[17] W/m^2. Also, Watson-Parris et al. (2025)[12] estimated an increase of +0.03 °C in the global mean temperature for the years 2020–2040, although this was accompanied by a 95% confidence interval of −0.09 to +0.19 °C.

In addition to light-scattering aerosols, marine vessels operated with conventional fossil fuel oils emit light absorbing PM—black carbon (BC) and brown carbon (BrC)[4,18,19], which contribute to atmospheric warming. Over regions with a high surface albedo, i.e., reflectivity, such as the Arctic[20], the warming effect of light-absorbing PM is amplified and continues when these particles deposit onto ice and snow[21]. Roughly two-thirds of Arctic BC emissions from shipping originate from HFO usage, whereas distillate-based fuels cover approximately the remaining third of the emissions[4]. Optical properties of ship aerosol emissions have previously been characterized for both directly measured engine exhaust emissions[18,19,22–24] and ship plumes[25,26]. These studies have shown that high-sulfur HFO typically emits particles with a high single scattering albedo (SSA), whereas low-sulfur fuels, such as distillates, have been shown to produce particles with a wide range of SSA values (0.35–0.98)[19,25]. Moreover, substantial amounts of BrC[19,23,24], and even infrared-absorbing BrC[18,27] have been observed in emissions of conventional HFO. However, most comprehensive characterizations on optical properties of ship emissions have been conducted prior to 2020 when low-sulfur residual fuels were not yet widely adopted, therefore the emission profiles and aerosol optical properties from these new hybrid fuels are largely unknown.

Particle emissions are often transported over long distances in the atmosphere, where they undergo atmospheric aging reactions (photochemical and dark aging). Photochemical aging, where transformation of atmospheric aerosol is governed by solar radiation and hydroxyl radicals (•OH), can lead to condensation of low-volatility oxidation products and surface changes on existing particles, inducing changes in the physical and chemical properties of particulate matter and thereby influencing the optical properties and radiative effects of the particles. Atmospheric aging can alter light absorption and scattering efficiencies of combustion aerosol particles, due to changes in the mixing state (e.g., lensing effect of non-absorbing coatings)[28–30] and particle morphologies (e.g., compaction of fractal aggregates)[31–33], and by the formation and transformations of BrC chromophores[34,35] and tarballs[36]. In addition to optical properties, coating formation on soot and compositional changes following atmospheric aging can affect the cloud activation potential of the particles[37–39]. Moreover, the effects of aging may largely depend on the emission source, requiring source-specific studies. While the effects of atmospheric aging on the optical properties of soot and other combustion aerosols have been previously studied[34,40–43], to the best of our knowledge, no detailed characterizations specific to ship emissions exist. For these reasons, it is critical to understand how atmospheric aging alters the radiative properties of emissions from marine vessels for accurately assessing their contribution to climate warming and for supporting policy decisions.

In this study, we characterized the optical properties of particulate emissions from a single cylinder research marine engine operated with marine fuels compliant with the current sulfur regulations. Further, we investigated the effects of photochemical aging on these emissions. Emission factors (EF) are provided, alongside details of particle morphology, mixing state, and radiative properties.

Results

Particle morphology and composition

Transmission electron microscopy (TEM) imaging showed the prevalence of soot in the fresh emissions of both the MGO and LS-HFO exhausts (Fig. 1). The soot-rich composition is also supported by the high mass fraction of refractory black carbon (rBC) (Fig. S1 and S2, Table 1). Tarball-like spherical particles were observed for most conditions, noting that it is not straightforward to visually distinguish between tarballs and spherical ash particles. Single-particle mass spectrometry (SP-MS) data showed complex particle compositions for both fuels. Fresh emissions generally contained either only elemental carbon (EC), combined organic carbon and elemental carbon (OC + EC), or all OC + EC + sulfur (S) signals in single particles detected by SP-MS (Fig. S3). In addition, calcium-rich particles likely originating from lubrication oil were identified from the single-particle data (Fig. S5).

Aging enhanced the non-refractory particle mass (nrPM, mainly organics and sulfates as shown by Fig. S1 and S2), by factors of 13.8 and 15.6 for LS-HFO and MGO, respectively, which resulted in a variety of particle morphologies, including coated and compacted soot, rods, and larger round particles. Formation of coatings on soot, as shown in Fig. 1f, where a dark and compact central particle with a surrounding ring of residue following vaporization of the coating under vacuum can be seen, is known to strongly impact optical properties by enhancing the light absorption efficiency of soot through optical lensing[44]. After aging, the majority of single particles exhibited OC, EC, and S signals (Fig. S3), indicating internal mixing between non-refractory particles and soot. Although particle hygroscopicity was not directly measured, the observed shift from fresh soot-rich particles to aged sulfate- and organic-containing particles suggests a likely increase in hygroscopicity and enhanced cloud activation potential. While spherical particles were visually abundant in the aged emissions, counts of typical tarball morphologies were too low to draw any definitive conclusions. Particles with rod- or needle-like morphologies made up a noticeable proportion of the aged MGO particles (Fig. 1f), but were rare in the aged LS-HFO samples (Fig. 1h), which instead contained particles similar to sulfates, supported by the high mass fraction of sulfates (Fig. S1 and S2). The abundance of rod morphologies in aged MGO exhaust is uncommon for exhaust aerosols, although similar rod- or needle-like morphologies have been observed in some previous studies of marine and other diesel engine emissions[45–49].

Figure 1i–j shows that MGO particles were roughly 25% smaller than those from LS-HFO, both in the fresh and aged emissions. Aging was accompanied by a decline in the projected area of around 10% for both fuels. For the fresh cases, the observed decline can be attributed to a reduction in the size of the soot in the exhaust. The decline with aging is attributed to the combination of the presence of smaller particles of different morphologies and the collapse of the soot[31], where the latter contribution is supported from inspection of the images.

Particle shapes were further quantitatively analyzed by means of defining circularity for the particles observed in TEM (Fig. 2). The fresh

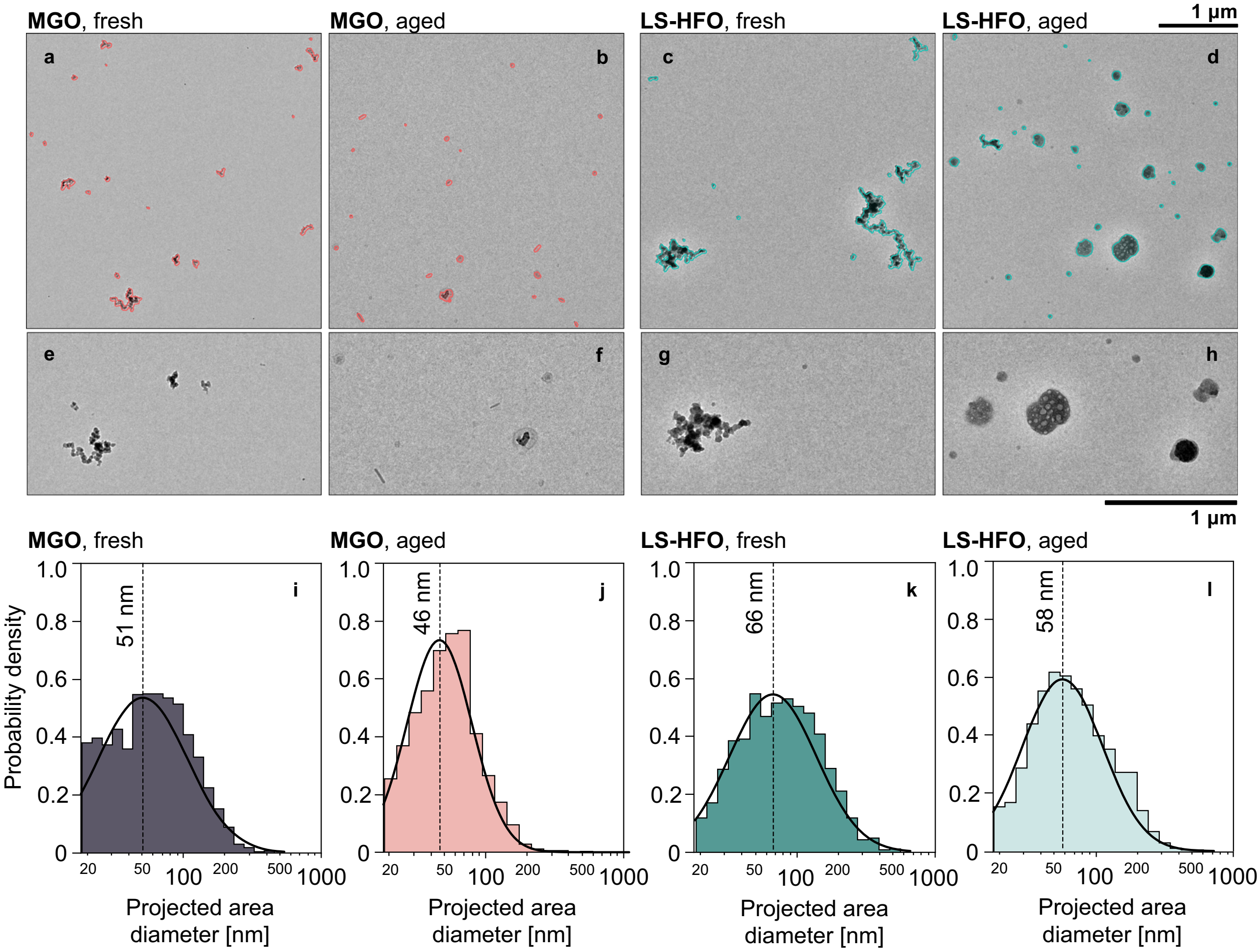

Fig. 1 | Particle morphology. a–h Representative TEM images for different fuels and aging. Top images show annotations corresponding to segmentation of the particles from the background using the *k*-means analysis procedure. Bottom images show a subregion of the top images without the segmentation mask. A common scale is used in all of the images in each row. **i–l** Projected area-equivalent diameter distributions of fresh and aged particles collected with different fuels. Vertical rules indicate the geometric mean diameter (GMD) following fitting of a lognormal distribution to the data. Size distributions are truncated on the left due to limitations in the automated segmentation algorithm. All cases shown are for 25% engine load.

samples exhibited broad distributions in circularity, consistent with the prominence of soot, which generally exhibits low circularity. Even in these cases, circularity tends towards unity for small soot aggregates, which are composed of fewer primary particles and thus naturally have more compact structures, resulting in a mode close to unity. Upon aging, the particle populations became more circular for both fuels. This change was more drastic for LS-HFO, which transitioned from larger soot aggregates to samples dominated by particles consistent with sulfates that have more spherical shapes than fractal aggregates. For MGO, the presence of rods in the images prevents a similar collapse in the circularity. Rods would be encountered in the middle of the panel ($\Phi = 0.3–0.7$), where the distribution is broader for MGO than LS-HFO. It is worth noting that inspection of Fig. 1 and similar images indicates that the automated algorithm tended to round out the mask applied to the rods, such that the true circularity is likely positively biased for the MGO particles.

BC mass absorption cross section and absorption enhancement

The 870 nm BC mass absorption cross section (MAC_{BC}) values from the full cycle were similar for both fresh MGO and LS-HFO, with a median of 5.4 (interquartile range, IQR 5.3–5.7) m^2/g. The MAC_{BC} remained relatively constant across different engine loads, except for the 25% engine load, where the median MAC_{BC} values were 6.1 (5.8–6.3) m^2/g (Fig. 3). The literature MAC_{BC} values for freshly emitted ship engine emissions have exhibited a range of 4.3–6.9 m^2/g (lower value by Aakko-Saksa et al. (2021)[50] and higher value by Corbin et al. (2018)[19]), when extrapolated to 870 nm with an assumed absorption Ångström exponent (AAE) of 1 for BC. The fresh MAC_{BC} in this work is in the middle of that range, whereas the aged MAC_{BC} ended up in a similar range to Corbin et al. (2018)[19]. The baseline MAC_{BC} value of 5.42 m^2/g was slightly below the upper bound of MAC of uncoated BC, 5.05 ± 0.44 m^2/g, reported in a recent review study by Liu et al. (2020)[51], as well as within the bounds of the value of $MAC_{BC} = 4.74 \pm 0.76$ m^2/g proposed by Bond and Bergstrom (2006)[52], with both values extrapolated from 550 to 870 nm with AAE = 1 (Fig. 3). Photochemical aging generally enhanced light absorption ($p = 0.013$ for 25% engine load, $p < 2 \times 10^{-16}$ for 50%, 75% and 100% loads), with absorption enhancement (E_{abs}) factors between 1.2 and 1.6. Opposite trends of E_{abs} were observed between MGO and LS-HFO in relation to engine load. For MGO, the highest absorption enhancement factor ($E_{abs} = 1.47$) occurred at 25% load. By contrast, for LS-HFO, the highest absorption enhancement ($E_{abs} = 1.56$) was seen at 100% load. For both fuels, these enhancements coincided with the highest enhancements of nrPM.

A positive correlation was observed between E_{abs} and total mass to BC mass ratio (M_{tot}/M_{BC}) (Fig. 4), where M_{tot} is the sum of nrPM and rBC mass. This ratio is a surrogate for coated particle mass in relation to BC in the case of internally mixed particles. Aged particles were likely internally mixed, as EC, OC and S signals were found in most of the analyzed single particles (Fig. S3). Positive correlation of E_{abs} as a function of M_{tot}/M_{BC} is primarily a strong indication of optical lensing due to the coating of soot with secondary

Table 1 | Optical properties and emission factors

			MGO, fresh					MGO, aged					LS-HFO, fresh					LS-HFO, aged				
	Engine load [%]		Full cycle	25	50	75	100	Full cycle	25	50	75	100	Full cycle	25	50	75	100	Full cycle	25	50	75	100
Optical properties	**MAC_{BC} (870) [m^2/g]**	Median	5.44	6.05	5.60	5.41	5.32	7.38	8.89	7.84	7.18	6.65	5.45	6.07	5.38	5.37	5.66	7.88	6.38	8.05	7.83	8.45
	E_{abs} (870)		1.00	1.12	1.03	1.00	0.98	1.36	1.64	1.45	1.33	1.23	1.01	1.12	0.99	0.99	1.05	1.45	1.18	1.48	1.45	1.56
	SSA (870)		0.17	0.17	0.13	0.16	0.21	0.22	0.29	0.23	0.19	0.22	0.22	0.25	0.20	0.22	0.27	0.35	0.37	0.40	0.33	0.36
	MAC_{PM} (870) [m^2/g]		4.94	3.44	4.89	5.01	4.91	3.32	1.02	1.75	3.54	3.59	4.56	4.29	4.83	4.57	4.37	0.77	0.83	0.78	0.81	0.42
	MSC_{PM} (870) [m^2/g]		1.13	0.75	0.88	1.16	1.56	0.92	0.44	0.54	0.96	1.13	1.33	1.33	1.19	1.32	1.67	0.40	0.50	0.51	0.40	0.25
	AAE (370/880)		0.98	1.19	1.01	0.97	0.95	1.06	1.36	1.11	1.05	1.03	0.95	1.28	0.97	0.93	1.00	1.07	1.25	1.01	1.04	1.12
	C (880)		3.18	3.95	3.40	3.12	3.04	2.80	3.68	3.26	2.79	2.65	2.93	3.52	3.09	2.90	2.90	2.72	3.52	2.74	2.69	2.83
Emission factors [mg/kWh]	**Total**	Mean	50.8*	112	84.2	34.4	20.9	159*	464	293	72.7	46.2	203*	735	319	78.9	28.8	952*	2590	1770	449	369
	rBC		43.2*	77.4	77.7	32.2	19.4	41.2*	61.6	70.0	33.8	22.9	144*	425	276	67.9	22.0	128*	402	232	56.8	20.0
	Total nrPM		7.54*	34.3	6.46	2.21	1.58	118*	402	223	38.9	23.3	59.8*	310	42.5	11.0	6.82	825*	2190	1540	393	349
	OA		7.19*	33.9	6.08	1.88	1.23	61.7*	255	92.5	15.6	8.39	55.3*	304	36.4	7.19	3.51	194*	820	238	54.8	40.6
	SO_4		0.32*	0.33	0.34	0.30	0.32	52.4*	134	124	21.9	14.1	4.27*	5.92	6.07	3.68	3.15	621*	1330	1290	333	304

*Weighted according to the ISO 8178-4 E2 cycle.

MAC_{BC} BC mass absorption cross section, *E_{abs}* absorption enhancement factor, *SSA* single scattering albedo, *MAC_{PM}* PM mass absorption cross section, *MSC_{PM}* PM mass scattering cross section, *AAE* Absorption Ångström exponent, *C* multiple scattering coefficient, *rBC* refractory black carbon, *nrPM* non-refractory particulate matter, *OA* organic aerosol, *SO_4* sulfate aerosol.

sulfates and organic matter in the PEAR, which is supported by the observed compaction of soot with increasing circularity after aging, shown in Fig. 2. The relationship was fit with an exponential function:

$$E_{abs,fit} = \left(\frac{M_{tot}}{M_{BC}}\right)^{0.17\,(\pm 0.03)}, \tag{1}$$

with a coefficient of determination of $R^2 = 0.77$. This formula was based on a fit to various experimental data sets by Chakrabarty & Heinson (2018)[53]:

$$E_{abs,fit} = \left(\frac{M_{tot}}{M_{BC}}\right)^{0.32\,(\pm 0.05)}, \tag{2}$$

which is accompanied by an exponent nearly twice as high as in the fit to the marine emission data in this work. Additionally, the results from this work fall within the wide range of values reported in literature (Fig. 4). To relate non-refractory particle mass to E_{abs}, previous studies have often expressed this relationship in terms of the non-refractory-to-BC mass ratio[28,41,54,55]. For comparability, all values were converted to M_{tot}/M_{BC}. In some of the studies[28,53,54], this ratio was derived with only BC-containing non-refractory particles, i.e. only the coating. However, studies that considered only coating mass did not always exhibit a steeper slope compared to those that defined the ratio using total non-refractory particle mass.

There was noticeable spread within the values of this work at high M_{tot}/M_{BC} ratios as well: 25% load with LS-HFO ($E_{abs} = 1.17$) is lower than other settings, while 25% load with MGO is higher ($E_{abs} = 1.66$). These differences can arise from variability in mixing states at different conditions, as fully encapsulated particles induce higher absorption enhancement than partially coated or externally mixed particles[56] and the ratio M_{tot}/M_{BC} does not discriminate mixing states. Considering this, it is possible that with MGO there were more encapsulated coatings exerting a stronger lensing effect, while for LS-HFO, the aerosol population was more heterogeneously mixed, which was qualitatively supported by the TEM images (Fig. 1). This was further supported by the single-particle data, where we saw a stronger enhancement of relative OC signals in EC-containing particles for the aged MGO compared to LS-HFO (Fig. S4), indicating that there were more BC-containing organics likely contributing to the lensing effect for MGO.

We also observed different non-refractory particle compositions at the low and high absorption enhancement points. This could play a role in the absorption enhancement, as the composition influences the refractive index, which can in turn influence optical lensing[57]. As an example, the lowest average value (LS-HFO 25% aged) had a high relative SO_4 mass fraction of nrPM ($SO_4 = 52\%$, $OA = 32\%$, $rBC = 16\%$), whereas the highest average value (MGO 25% aged) corresponded to a higher relative OA mass fraction ($SO_4 = 29\%$, $OA = 55\%$, $rBC = 13\%$). Also, within OA, the real part of the refractive index has been shown to vary between 1.3–1.7[58].

Single scattering albedo and simple forcing efficiency

The 870 nm single scattering albedo (SSA), determined by the scattering (b_{sca}) and absorption coefficients (b_{abs}) measured by the photoacoustic extinctiometer (PAX),

$$SSA = \frac{b_{sca}}{b_{abs} + b_{sca}}, \tag{3}$$

resulted in values between 0.2–0.3 and 0.15–0.25 for fresh LS-HFO and MGO emissions, respectively. Similar values have been reported for uncoated soot particles, e.g. values between 0.15 and 0.29 were reported in a review by Bond and Bergstrom (2006)[52]. Due to the high mass fraction of BC in freshly emitted particles in this work, similar SSA values to bare soot were expected. Photochemical aging generally increased SSA ($p = 0.013$ for 100% engine load, $p < 2 \times 10^{-16}$ for 25%, 50% and 75% loads). With MGO, aging increased the SSA values on all engine loads except for 100% load (Fig. 5a). With LS-HFO, the increase in SSA was observed at all loads, leading to

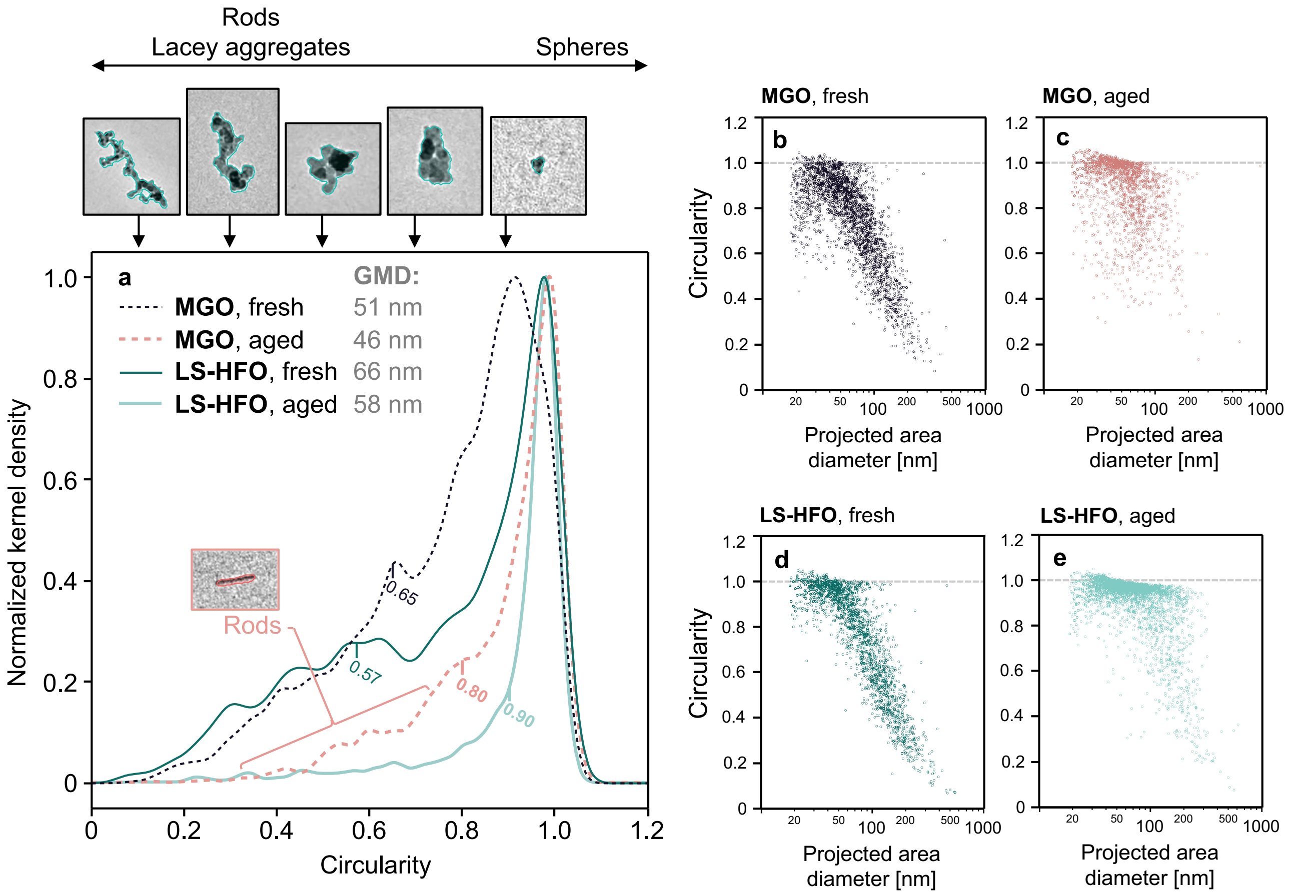

Fig. 2 | Particle circularity. a Normalized kernel densities of circularity. Electron microscopy images above the panel show example particles at circularities of 0.1, 0.3, 0.5, 0.7, and 0.9, in ascending order. The 25th quartiles are highlighted for each curve. **b**–**e** Particle circularity versus projected area diameter. Horizontal dashed line corresponds to a value of unity, which corresponds to a circle. All cases shown are for 25% engine load.

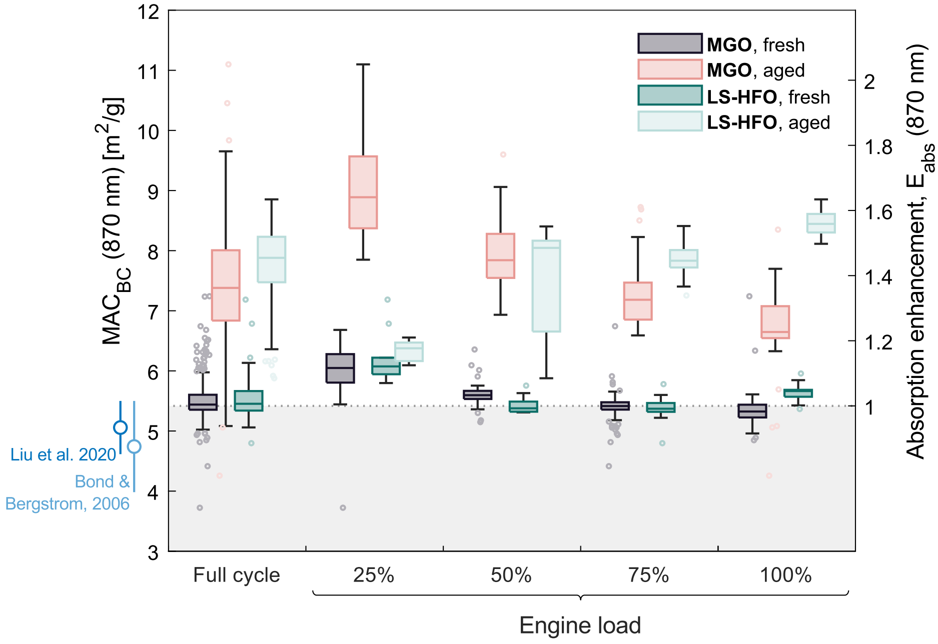

Fig. 3 | BC mass absorption cross section and absorption enhancement at 870 nm wavelength. Boxes correspond to data between upper and lower quartiles, middle lines indicate medians, whiskers correspond to non-outlier maximum and minimum values, and light dots indicate outliers. Boxes of different colors left to right: MGO fresh, MGO aged, LS-HFO fresh and LS-HFO aged. The shaded area with dashed horizontal line represents a MAC_{BC} of 5.42 m^2/g for the median of ≥75% engine loads, corresponding to no absorption enhancement. Markers on the left side of the plot show uncoated MAC_{BC} from two review articles: 5.05 ± 0.44 m^2/g[51] and 4.74 ± 0.76 m^2/g[52].

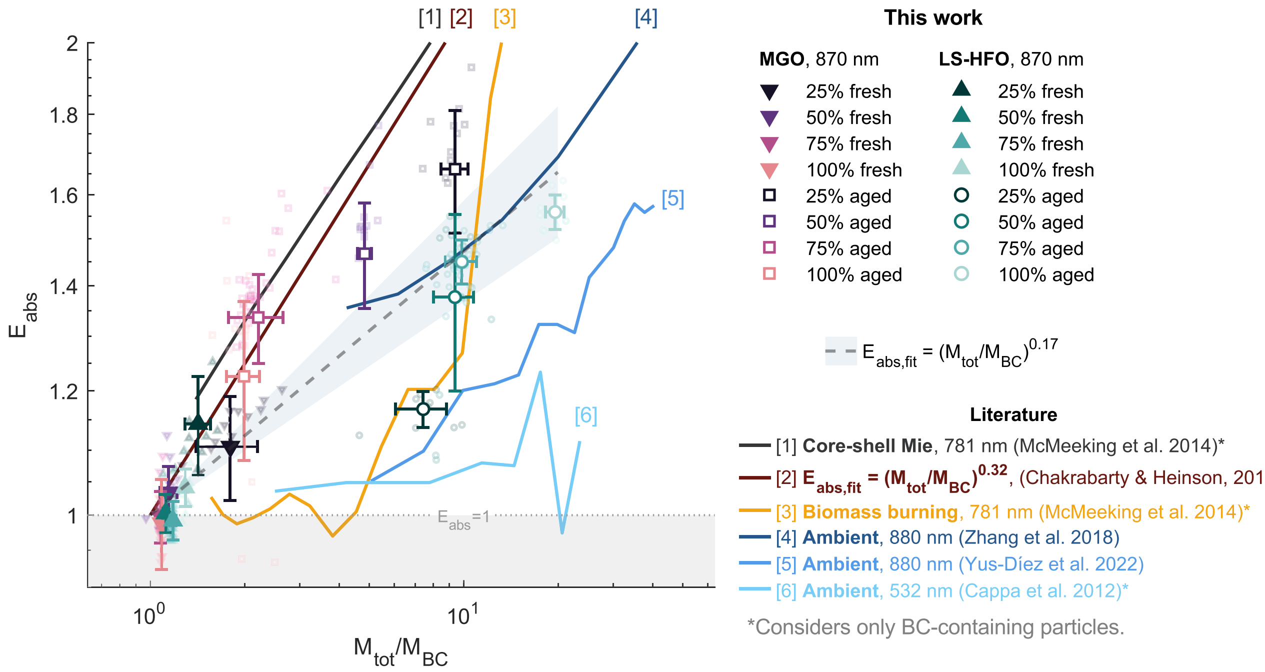

Fig. 4 | Absorption enhancement (E_{abs}) as a function of total mass to BC mass ratio (M_{tot}/M_{BC}). In this work, M_{tot} is nrPM+rBC; nrPM is primarily organics and sulfates measured by AMS, and rBC from LII. Non-transparent markers represent averages and error bars represent standard deviations, whereas smaller transparent markers show individual points of time-resolved data. Marker colors correspond to the engine load (%). Dashed line shows the log-log fit to average values from this work. Shaded region with the horizontal dotted line is $E_{abs} = 1$, indicating no absorption enhancement. Values from literature[28,41,53–55] are shown as connecting solid lines.

values between 0.3–0.4 in the aged samples, which is likely due to higher quantities of secondary sulfates. Thus, aging enhanced light scattering slightly more than light absorption at 870 nm. Nevertheless, SSA values below 0.5 mean that light absorption was stronger than scattering.

The SSA values obtained in this work are generally lower than in previous studies from ship engines. For LS-HFO, the fresh SSA (870 nm) range of 0.2–0.3 is considerably lower than values between the range 0.5–0.9 (780 nm) reported for a high-sulfur HFO in Corbin et al. (2018)[19]. For LS-HFO, this is likely a result of reduced emission of fresh sulfates. However, the MGO SSA varied between 0.53–0.98 in Corbin et al. (2018)[19], which is substantially higher than MGO SSA measured in this work (Table 1, Fig. 5a). The higher SSA observed by Corbin et al. (2018)[19] is likely caused by the combination of (1) a higher OA/BC ratio (Figs. S9), (2) externally mixed non-soot particles, (3) larger particle size and (4) instrumental differences. To elaborate on these points, (1) organics emitted from marine engines can vary when the same fuel is used, substantially influenced by unburnt lubrication oil[59], (2) Corbin et al. (2018)[19] showed that the freshly emitted organics were largely externally mixed, and external mixtures have been shown to exhibit higher SSA values than coated soot[60], (3) increasing particle size in sub-micron particles generally corresponds to higher scattering cross sections and single scattering albedos, and (4) extinction-minus-scattering, the method used in Corbin et al. (2018), and PAX, used here, have exhibited different SSA values in a previous intercomparison[61]. Another study by Lack et al. (2009)[25] reported SSA (532 nm) values measured from ship plumes, exhibiting an average value of 0.6 for high-sulfur fuels. However, in the same study the corresponding SSA was 0.35 for low-sulfur fuels, which is closer to the values observed in this work (Table 1; Fig. 5a).

The potential radiative effects due to aerosol-radiation interactions, i.e. the direct radiative effect, by the particle emissions were assessed using the spectral Simple Forcing Efficiency (SFE)[62,63]:

$$\frac{dSFE}{d\lambda} = -\frac{1}{4}\frac{dS(\lambda)}{d\lambda}\tau_{atm}^2(\lambda)(1-F_c)\left[2(1-a_s)^2\beta(\lambda)\cdot \mathrm{MSC_{PM}}(\lambda) - 4a_s\cdot \mathrm{MAC_{PM}}(\lambda)\right], \qquad (4)$$

where $dS/d\lambda$ is the solar irradiance (in W/(m^2 nm)), τ_{atm} the atmospheric transmission (0.79), F_c the cloud fraction (0.6), a_s the surface albedo, β the backscatter fraction, MSC_{PM} the mass scattering cross section of PM (in m^2/g) and MAC_{PM} the mass absorption cross section of PM (in m^2/g). MAC_{PM} and MSC_{PM} were defined as absorption and scattering cross sections per total PM (nrPM+rBC). Spectral light absorption data was measured by the aethalometer, whereas light scattering, measured by PAX, was extrapolated from 870 nm using a scattering Ångström exponent (SAE) of 2, and the SAE range 1–3 was included as a range of uncertainty. To account for the effect of emitted mass, SFE values were weighted by the PM emission factors (W/g * g/kWh). Backscatter fraction of 0.25 was used in the following discussion, and a range of realistic backscatter fractions between 0.15–0.35 was investigated as a sensitivity test since backscattering is not measured by PAX. SFE serves as a simplified metric to compare the direct radiative forcing effect between fuels and aging conditions, while it does not account for the temporal and spatial variability of ship plumes in the real atmosphere, or for the underlying clouds and aerosol-cloud interactions.

Fresh particle emissions from both fuels exerted a positive radiative forcing over most surface albedos, as shown in Fig. 5d. LS-HFO had a 3.6 times higher SFE than MGO over a surface albedo of 0.8, representing fresh snow and ice. Over the global average surface albedo ($a_s = 0.19$), LS-HFO exhibited 3.4-fold higher SFE compared to MGO, and a 2.1-fold higher SFE over ocean ($a_s = 0.06$). SFE values on snow/ice were largely independent on the backscatter fraction and SAE due to the minimal scattering term, whereas over low surface albedos, the backscatter fraction and SAE had an increasing influence on the result.

For MGO, aging increased the SFE values by 16% over ice/snow, by 8% over the global average, and decreased the SFE by 41% over ocean. After aging, LS-HFO SFE was reduced by 28% over ice/snow, by 41% over the global average, and it decreased from 3.1 to −2.6 W/kWh over ocean. Reduction of LS-HFO SFE after photochemical aging is likely related to a higher degree of secondary sulfate formation and lower relative E_{abs} compared to MGO. After aging, LS-HFO SFE was 2.2 times higher than for MGO over ice/snow and 1.8 times higher over the global average.

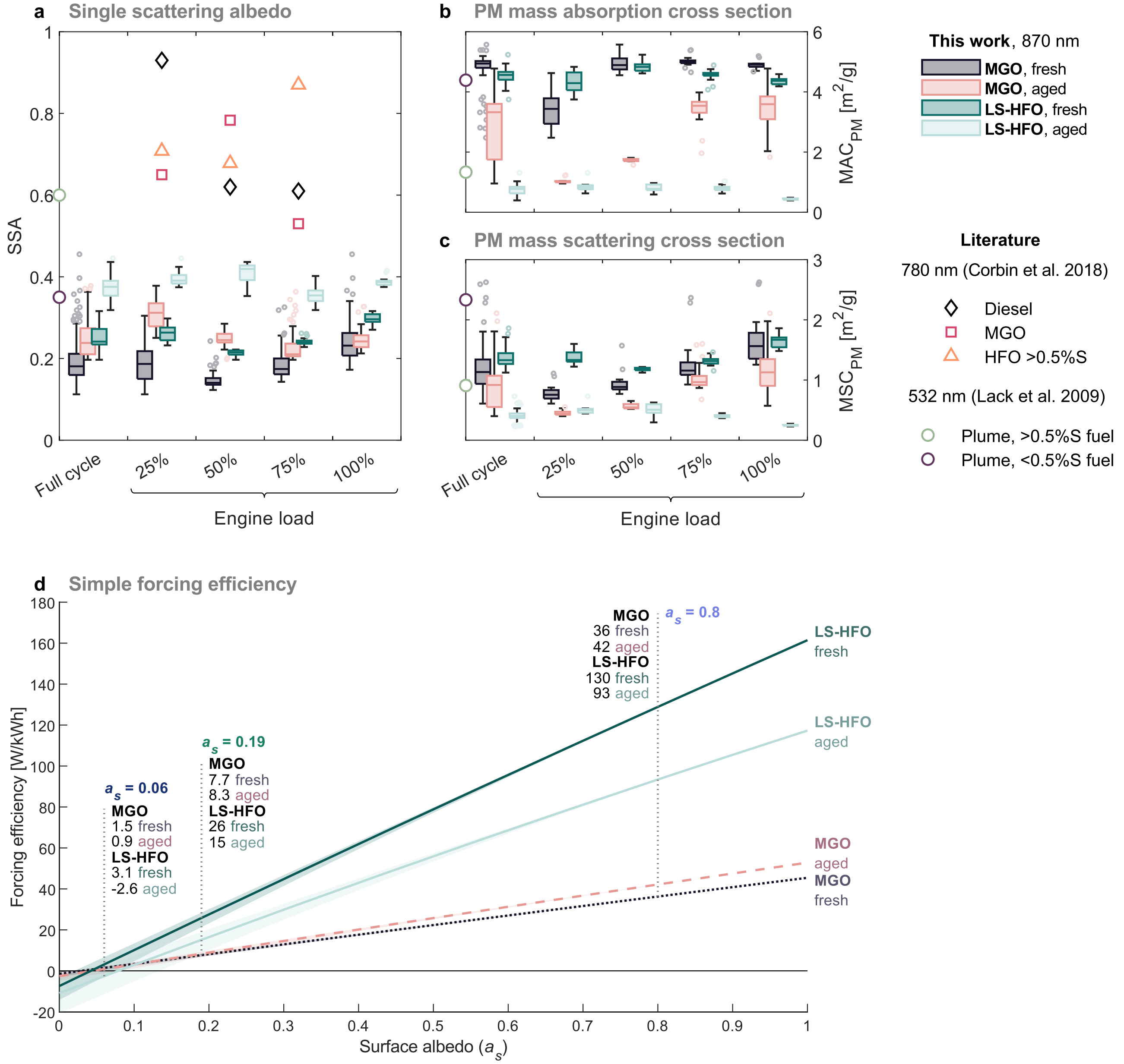

Fig. 5 | Radiative properties of particulate matter. a Single scattering albedo, **b**, **c** mass absorption and scattering cross sections of PM. Boxes correspond to data between upper and lower quartiles, middle lines indicate medians, whiskers correspond to non-outlier maximum and minimum values, and light dots indicate outliers. Boxes of different colors left to right: MGO fresh, MGO aged, LS-HFO fresh and LS-HFO aged. Literature values are shown as single points for comparison[19,25]. **d** Simple forcing efficiency (in W/kWh) using full cycle MAC_{PM} and MSC_{PM} values and PM emission factors. The shaded areas depict the sensitivity of SFE to backscatter fractions between 0.15–0.35 and scattering Ångström exponents between 1–3, as these two parameters were not measured. Surface albedos of 0.06, 0.19 and 0.8 are highlighted, as they represent values for ocean, the global average and ice/snow, respectively.

Wavelength dependence of light absorption

Absorption Ångström exponents (AAE) defined for fresh MGO and LS-HFO emissions using the wavelength pair of 370/880 from AE33 had medians of 0.98 (0.96–1.01) and 0.95 (0.93–1.02) during full cycles, respectively, generally corresponding to literature values reported for marine distillate fuels. As AAE hovered around ~1 during to full cycle, light absorption was almost entirely attributed to BC. Extrapolating Aethalometer IR absorbance with AAE = 1 to short wavelengths and subtracting it from the total 370 nm absorption resulted in 15–30% BrC absorption at the 25% engine load, with noticeable absorbance at the visible light region (Fig. S10). In addition to BrC attribution from AE33, UV-vis analyses were conducted from methanol extractions of filter samples to observe the absorbance of methanol-soluble organic carbon (MSOC). MSOC absorption had a higher wavelength dependence than BrC derived from AE33, and it accounted for only ~2% of total light absorption at 370 nm (Fig. S10). The discrepancy between the online and offline method indicates that fresh BrC from both fuels is mostly insoluble in methanol. Emissions from LS-HFO in this work generally exhibited lower AAE values compared to those reported for >0.5% S HFO in literature (Table S3, Fig. 6), indicating that LS-HFO emissions may have a wavelength dependence more similar to distillate fuels than to conventional HFO.

An increase of 0.08 to AAE = 1.06 (1.03–1.11) was observed for photochemically aged MGO emissions during the whole cycle, while LS-HFO AAE increased by 0.06, leading to AAE = 1.07 (1.03–1.13). It is likely that the minor increase in AAE ($p < 2\times10^{-16}$) was caused by optical lensing, as coating of soot with non-absorbing material has been modeled to result in values as high as 1.25–1.4[64,65]. For MGO, aging caused the highest increase in AAE at 25% engine load but showed no distinguishable difference between

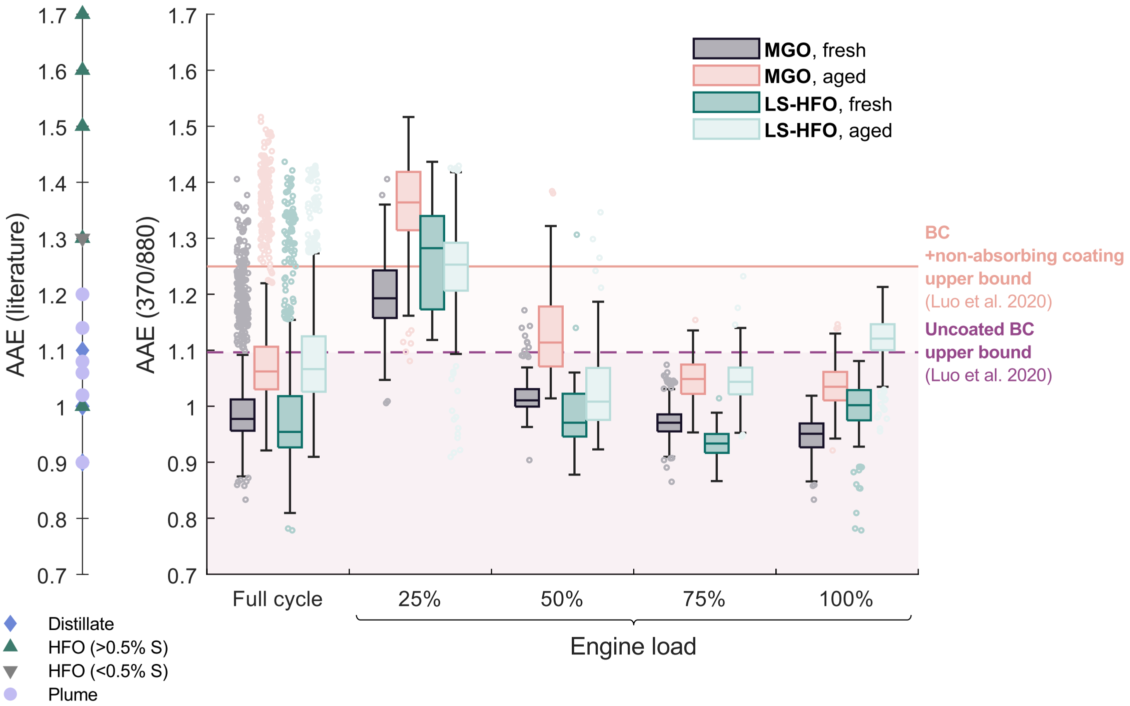

Fig. 6 | Absorption Ångström exponents, i.e. the wavelength dependence of absorption. Left axis shows literature values, taken from Table S3[19,23,24,26,70]. Horizontal lines indicate modeled upper limits for uncoated BC and BC with a non-absorbing coating[64]. Boxes correspond to interquartile ranges, middle lines indicate medians, whiskers correspond to non-outlier maximum and minimum values, and light dots indicate outliers. Boxes of different colors left to right: MGO fresh, MGO aged, LS-HFO fresh and LS-HFO aged.

fresh and aged MSOC absorption (Fig. S11), suggesting that the AAE enhancement occurred mainly due to non-absorbing coatings. Also, as shown in Fig. S12, the ratio between fresh and aged absorption coefficients increased relatively uniformly across all wavelengths after aging, highlighting that the lensing effect is more significant in regards to the total light absorption. The results indicate that fresh BrC emitted from marine engines is mostly inert to photochemical aging, and that coating of soot is the key mechanism inducing changes in the light absorption by these particles.

Multiple scattering coefficients

Multiple scattering coefficients (ratio of light attenuation from Aethalometer (AE33) and light absorption from Photoacoustic Extinctiometer (PAX)) exhibited median values between 2.44 and 3.64 across different engine loads. A substantial engine load dependency of the multiple-scattering coefficient was observed, with C being higher at the lowest engine load settings (Fig. 7). Furthermore, aging decreased C values ($p = 0.12$, $p = 0.0092$, $p < 2 \times 10^{-16}$ and $p = 0.13$ for 25%, 50%, 75% and 100% loads, respectively). Due to these effects, applying any constant value for C includes uncertainty in the absorption and BC mass defined with filter-based photometers. $C = 3.00$, which was the median value in fresh emissions during engine loads ≥75% was used for b_{atn} to b_{abs} conversion, therefore the equivalent black carbon (eBC) derived from these conversion factors will contain positive bias on low engine loads. AE33 data with the default conversion parameters ($C = 1.39$ and $\mathrm{MAC_{BC}}$ (880 nm) = 7.77 $\mathrm{m^2/g}$) would've resulted in a ~ 40% overestimation compared to data with experimental C and $\mathrm{MAC_{BC}}$ values. As default conversion parameters are commonly used, eBC values given by the instrument may contain considerable positive bias. AE33 and PAX were on two separate dilution ratios, AE33 in 1:1000 and PAX in 1:100. Comparison of SMPS particle volumes in 1:100 versus 1:1000 dilutions showed a mean relative error of 2.49% with no distinct bias on any engine loads (Fig. S14), concluding that the bias in C was not a result of inaccuracies in the excess dilution.

Multiple scattering coefficients have been previously defined for marine emissions by Corbin et al. (2018), where an average C of 4.7 was observed, with substantial variation between average values of 3.5–9.5. Most commonly, C has been determined from atmospheric measurements[66–69], for example; $C = 3.6$ in Backman et al. (2017)[66], $C = 2.39$ in Yus-Díez et al. (2021)[68], suggesting that the manufacturer's default value used by the AE33, $C = 1.39$, is a significant underestimation. These studies also reported that multiple scattering coefficients include considerable variation under different experimental conditions[19,66], agreeing with the findings in this work and suggesting that a constant C value for complex aerosol mixtures can be a significant source of uncertainty for filter-based photometers. The light absorption inferred from filter-based attenuation can be positively biased if the filter is loaded with aerosols with high SSA[68]. This was not the case in this work, as the particles were highly light-absorbing (a maximum SSA of 0.43, with typical values between 0.1 and 0.3).

BC emission factors

BC emission factors (EF) exhibited a substantial dependence on the engine load and the fuel (Fig. 8). On average, during the full cycles, time-weighted average BC EFs from LS-HFO were 3x higher than MGO. The difference between BC EFs from LS-HFO and MGO was highest at the 25% engine load, with LS-HFO BC EFs 4.6 times higher than MGO. With increasing engine load, EFs with both fuels decreased and converged in relation to each other, so that on the 100% engine load LS-HFO BC EFs were only higher by a factor of 1.1. Thus, if both fuels are used under high loads, the emitted BC masses would be very similar in relation to the output energy from the engine. However, at low loads, MGO emitted considerably less per unit of output energy than LS-HFO.

BC EFs from MGO were mostly within the same range as literature EFs from distillate shipping fuels. Prior to 2020, the global FSC limit had been 3.5%, thus multiple earlier publications have studied HFO with a higher FSCs than now. However, in recent studies, IMO 2020 compliant low-sulfur residual fuels were also studied[70,71], where BC EFs of LS-HFO have been in a

Fig. 7 | Aethalometer multiple scattering coefficients (*C*). **a** MGO fresh, **b** LS-HFO fresh, **c** MGO aged, **d** LS-HFO aged. Descending x-axes correspond to increasing engine loads. Vertical lines indicate median values, also shown in the column on the right.

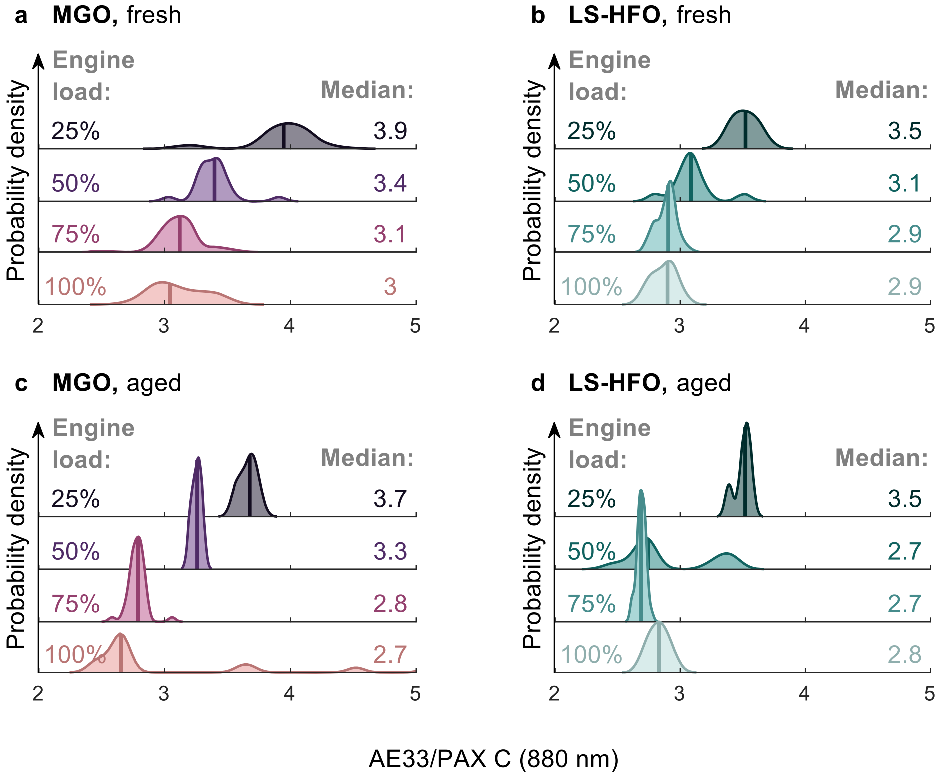

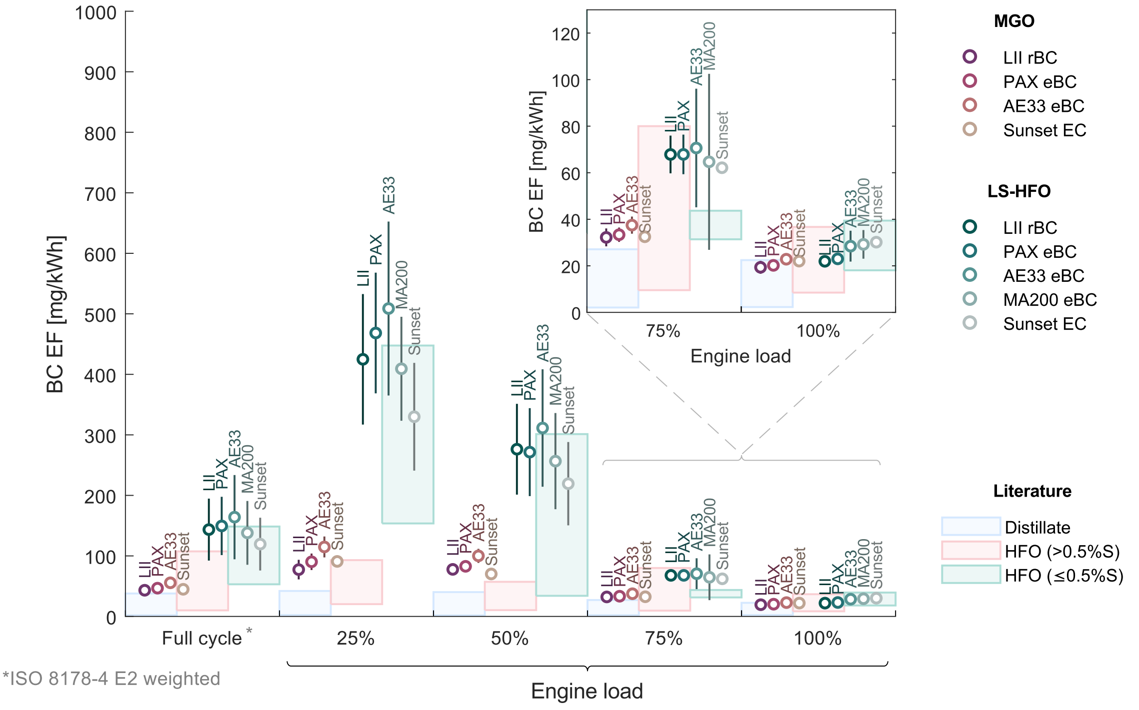

*ISO 8178-4 E2 weighted

Fig. 8 | BC emission factors (BC EF) specified by engine load and defined using different methods; LII rBC, PAX eBC, AE33 eBC, MA200 eBC and Sunset EC. Points represent average values, and error bars standard deviations. E2 weighted averages and standard deviations are shown for the full cycle. 75% and 100% engine loads are truncated in the subplot at the top right corner to improve visibility on the low y axis values. Boxes in the background represent the interquartile range of literature EFs for distillate fuels, non-compliant (>0.5%S) and compliant (≤0.5%S) HFO (Table S2).

similar range to this work (HFO ≤ 0.5%S in Fig. 8). Comparing the results to previous studies indicates that low-sulfur HFO can emit as much or even higher quantities of BC than high-sulfur counterparts (Table S2, Fig. 8).

The aethalometer, which is one of the most commonly used atmospheric BC measurement instrument, and which has previously been used to define BC emissions from marine engines[50,72], had a bias in eBC mass depending on the engine load, as it is directly influenced by the bias in *C*. The uncertainties associated with using constant values for the analysis (*C* and MAC_{BC}) should be acknowledged when using aethalometer to define emission factors, as these parameters change depending on operation conditions and photochemical aging. This is likely the case also for other filter photometers, such as the commonly used Filter Smoke Number (FSN) method. The aethalometer's high sensitivity required substantial dilution of the marine emissions to stay within the optimal measurement range, which would require more complex measurement setups if the device was to be used more routinely. High dilutions are also a source of elevated uncertainty. For photoacoustic light absorption, the main BC measurement uncertainty is related to using a constant value for MAC_{BC}, which was observed to increase after photochemical aging and to lead to potential overestimations of up to 1.6 times. Overall, absorption enhancement by non-absorbing compounds should be considered when interpreting eBC results from any optical absorption measurements.

Laser induced incandescence was considered to be the most robust option for BC mass determination and the reference to which other instruments were compared to, as it is a more direct measure of mass and largely independent of particle mixing state. However, there are uncertainties associated with coatings during laser heating, which could change the peak incandescence and thus the retrieved mass[73]. Thermal-optical EC determination as BC also has the advantage of being a direct mass measurement, albeit not capable of producing high temporal resolution data like the other instruments used here. The EC method still has uncertainties related to sample handling and storage, low detection limits (corresponding to long sampling times), as well as to the optical split-point for determining pyrolytically converted carbon[74–76]. The split point accuracy can however be optimized by having a filter EC mass loading within the manufacturer's recommended range of 1–15 μg/cm^2 to get a good baseline measurement, as well as having the OC mass loading within the recommended range of 5–400 μg/cm^2 to avoid excessive charring. Beyond conventionally defined BC and BrC, ship emissions may contain intermediate carbonaceous tar-like BrC particles[18], which have a high degree of insolubility and refractoriness, as well as light absorption extending up to near-IR wavelengths. Due to its properties, tar BrC can bias the BC concentrations depending on the measurement method. For example, near-IR absorption by tar BrC can lead to overestimation of absorption-based BC. Techniques to quanitify tar BrC would need to be further developed in order to get closure on the light-absorbing aerosols emitted by shipping[18,27].

Discussion

The fresh marine engine emissions with both fuels were primarily composed of black carbon, and the optical properties (MAC, AAE, SSA) were similar to those of uncoated soot. In terms of optical properties, LS-HFO aerosol emissions resembled more those of distillate fuels than conventional HFO. TEM images affirmed the dominance of soot in the fresh samples and a transition to compact and coated soot, as well as other diverse particle morphologies after aging. MGO and LS-HFO showed different types of particles after aging, with LS-HFO having particles likely containing sulfates, while rod-like morphologies were seen with MGO. Photochemical aging had an increasing effect on BC mass absorption cross sections, which was attributed to optical lensing by coatings formed in the photochemical aging reactor. After photochemical aging, the AAE was slightly enhanced. This was hypothesized to result from the lensing effect rather than by changes in BrC. LS-HFO had a 2–3.5-fold higher forcing efficiency compared to MGO. For MGO, the forcing efficiency remained mostly unchanged after aging, whereas for LS-HFO, the forcing efficiency decreased relative to fresh emissions. In most cases, the forcing efficiency was positive, even after photochemical aging.

Overall, the different BC measurement methods showed good agreement when measuring fresh emissions where the aerosol particles mostly consisted of BC, whereas the differences between instrument responses were magnified after photochemical aging, as the particle properties influencing the conversion factors became more complex. The main things to consider concerning optical determination of eBC are the impacts of absorption enhancement, which can lead to overestimation of BC mass when these particles are coated, and a "default" MAC_{BC} value for uncoated BC is used. Further, with filter-based absorption photometers, the interaction between the sample and the filter matrix has been shown to cause measurement bias, which is not straightforward to account for without reference instrumentation. Nevertheless, by using appropriate conversion factors, filter photometers resulted in very comparable BC data from ship emissions.

Current global regulations on FSC in marine fuels aimed at addressing environmental and health issues regarding sulfur pollution, while black carbon emissions from the marine sector still presents an unresolved issue under current marine legislation. The results combined with literature values suggest that the use of low-sulfur residual fuels may release as high or even higher quantities of black carbon than previously commonly used high-sulfur heavy fuel oils. The lower SSA values for low-sulfur HFO—a result of lower sulfate emissions in the fresh exhaust—when compared to prior research with >0.5% S residual fuels suggests that IMO 2020 compliant LS-HFO exerts a stronger positive radiative forcing effect than high-sulfur HFO. Furthermore, the possibility that BC emissions remain high after IMO 2020 regulations is compounded by the net warming effect resulting from reduced sulfate-driven cooling[12–15,77].

The results of this study provide a basis for improved assessments of the aerosol–radiation interactions (ARI) from marine traffic under the current fuel sulfur regulations, while accounting for the effects of photochemical aging. The ARI forcing efficiency estimates presented in this work were based on a simplified model which allows for straightforward comparisons between sources with different optical properties. However, the model does not factor in the vast spatiotemporal variability in the exhaust emissions or the radiative effect due to aerosol-cloud interactions (ACI), therefore it should not be single-handedly used to derive the global radiative forcing effect. Our findings highlight the need for further studies, including field and laboratory measurements of different marine vessels and new marine fuels (e.g. biofuels, ammonia [NH3] and methanol), smog chamber experiments to study emission transformation under more realistic aging conditions, atmospheric modeling and investigations on ACI, to better understand the atmospheric impacts of ship emissions and to identify sustainable marine propulsion technologies and alternatives to conventional shipping fuels.

Methods

Experimental setup

Experiments were conducted on a laboratory-based 4-stroke single-cylinder medium-speed research engine, which has been described in multiple previous studies[19,24,70,78,79]. In short, the engine featured a 150 mm bore and 180 mm stroke and was operated at the rated 1500 rpm speed with stable engine load steps 25%, 50%, 75% and 100% of the 80-kW nominal power output of the engine. The engine loads and their respective durations were based on the ISO 8178-4 E2 standard test cycle (Table S4). Each experiment consisted of two consecutive test cycles; first conducted with increasing engine load, and the second with decreasing load.

The engine was operated with marine gas oil (MGO) and low-sulfur heavy fuel oil (LS-HFO). The MGO is a distillate-based shipping fuel with a FSC of 0.01%, making it appropriate for SECAs. The LS-HFO is a highly viscous residual fuel oil that has a FSC of 0.5% and is therefore in accordance with the global sulfur limit of 0.5% set in 2020 by IMO. The properties and elemental composition of the marine fuels have been published elsewhere[80,81]. The NOx EFs were on average 5 g/kWh[81], meaning that the engine complied with the Tier II classification (< 8 g/kWh) at 1500 rpm rated speed. However, the engine did not meet the Tier III limit (< 2 g/kWh), which is in use for NOx Emission Control Areas (NECA).

Exhaust emissions were sampled through a heated line (350 °C) into a pre-cyclone (10 μm diameter cut-off) and a two-diluter setup, consisting of a porous tube diluter and an ejector diluter (DAS, Venacontra), and resulting in a combined dilution ratio (DR) of 1:100 (Fig. 9). The real-time DR was automatically adjusted with an custom-built dilution controller, which determined the ratio based on three simultaneous measurements of CO_2 concentrations in the raw exhaust, dilution air and the diluted sample. After dilution, the aerosol sample was either directed through the Photochemical Emission Aging flow tube Reactor (PEAR)[82], here referred to as "aged", or alternatively a "fresh" bypass sampling line without aging. The sample was

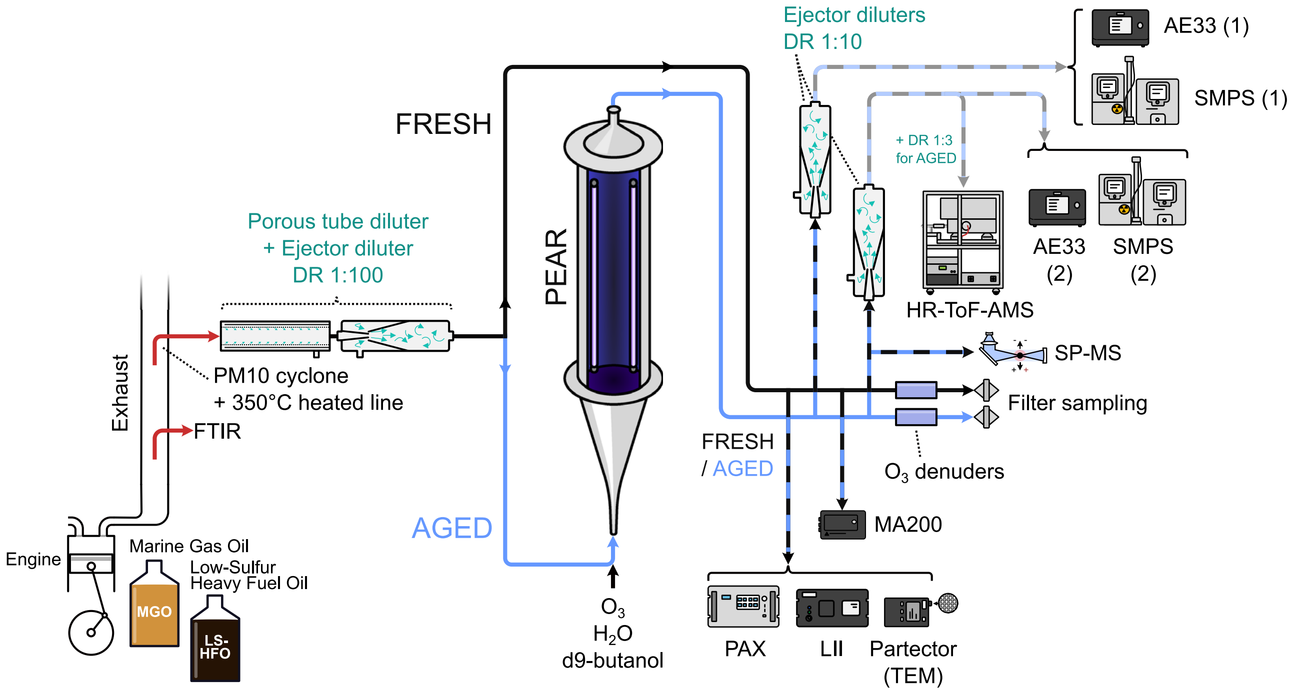

Fig. 9 | Representation of the sampling setup. Black-blue-striped lines indicate sampling lines that were measuring only the fresh or aged sample at a time. Quartz filters were collected simultaneously from the fresh and aged channels. Instrument abbreviations: FTIR fourier transform infrared spectrometer, PAX photoacoustic extinctiometer, LII laser-induced incandescence, MA200 microaethalometer, HR-ToF-AMS high-resolution time-of-flight aerosol mass spectrometer, SP-MS single-particle mass spectrometer, AE33 aethalometer and SMPS scanning mobility particle sizer.

also diluted by a constant factor of 1:10 with an ejector diluter for some instruments, and further by a factor of 1:3 with aged emissions for the high-resolution aerosol mass spectrometer (HR-ToF-AMS).

For filter sampling, the exhaust stream was split into the sampling line of the filter and gas phase sampling setup. High purity Quartz Fiber Filters (47 mm, QFF, Whatman QM-A, Cytiva) were used for the particle collection. QFFs were baked for 5 h at 550 °C prior to sampling to remove possible contaminants. Partisol Model 2300 Speciation Sampler (Rupprecht & Pataschnick Co., Inc.) with a sharp-cut PM2.5 impactor was operated for 240 min at 10 l/min accounting for a total volume of 2400 l. The filter samples were then kept in Analy slide petri dishes (Pall Corporation) and stored in a freezer at −20 °C until conducting the analyses. The aged exhaust was passed through ozone denuders upstream to the particle/gas phase sampling. The denuders consisted of ceramic honeycombs which were impregnated with potassium nitrite to decompose ozone in the sample.

Exhaust particles were also sampled onto carbon-coated copper grids for transmission electron microscopy (TEM) with an electrostatic precipitator sampler (Partector 2, Naneos). The volumetric flow rate of the sampler was 0.5 l/min. Imaged particles were segmented from the background using a custom *k*-means algorithm, described in a previous work by Sipkens and Rogak (2021)[83], allowing for per-particle statistics including projected area-equivalent diameter. Particle compactness was quantified using circularity (Φ), which considers the ratio of projected area to the perimeter:

$$\Phi = \frac{4\pi A}{P^2}, \tag{5}$$

where A is the projected area of the shape and P is the perimeter of the shape. This quantity captures the compactness of the particles, with spheres having circularity values approaching unity and fractal aggregates having substantially lower values. While the circularity should only vary between 0 and 1 in theory, image rastering (i.e., the use of pixels) to represent the perimeter and area can result in circularities that exceed 1 in practice.

Photochemical aging

The PEAR, a high-volume oxidizing flow tube reactor[82], was used to create photochemical aging conditions for the exhaust sample. Four ultraviolet (UV, 254 nm) lights located inside the PEAR can be individually turned off or adjusted up to 10 V per lamp. Lamps were operated at full 4x10V voltage to achieve between 1–5 equivalent days (eqv.d) of photochemical age, depending on the engine load. The UV lights were surrounded by a cooling case built from quartz tubing to negate the effects of elevated temperature, such as changes in the partitioning of semivolatile compounds or decreased relative humidity. The sample flow through PEAR was 100 l/min with a residence time of 70 s.

Ozone (O_3, 4–7 l/min), water vapor (H_2O, humidifier 9 l/min, +50 °C), and d9-butanol (8–30 ml/min) were continuously fed into PEAR. Within PEAR, O_3 photolysis by UV light creates short-lived oxygen radicals (O(1D)) that subsequently react with H_2O, resulting in hydroxyl radicals (•OH), which is the main oxidant during day. The OH exposure was monitored with a proton-transfer mass spectrometer (PTR-MS) that measured the decay of the OH tracer d9-butanol[84]. The equivalent photochemical age was calculated for the ambient concentration of $[OH] = 10^6$ molec./cm^3. The feeding of reactants introduced an internal dilution of 10% in the PEAR, which was accounted for in data processing.

Measurement of optical properties and black carbon

The Photoacoustic Extinctiometer (PAX, Droplet Measurement Inc.) was used to measure scattering and absorption by aerosol particles at 870 nm wavelength. In the PAX, the sample flow is split into two cells of the instrument, the scattering and absorption cell. In the absorption cell, a modulated laser is directed at the sample aerosol, which re-emits the radiation as heat in the presence of light absorbing particles. This heat creates pressure waves at the laser's modulation frequency, which is set as the resonant frequency of the photoacoustic cavity. The sound created by the absorbing particles is picked up by a sensitive microphone, and the amplified signal is proportional to the absorption coefficient[85]. The scattering cell consists of an integrating reciprocal nephelometer, measuring light scattering from 6 to 174°[86]. With the simultaneous light absorption and scattering measurements, SSA values were also obtained. The scattering and absorption calibrations were conducted prior to the measurement campaign. The scattering signal was calibrated using nebulized non-absorbing ammonium sulfate particles, whereas the light absorption signal was calibrated using nebulized absorbing Aquadag particles. For PAX, a flow rate of 1 l/min was used and the total dilution ratio at the sample inlet was 1:100.

Two Aethalometers (AE33, Magee Scientific) and two Microaethalometers (MA200, AethLabs) were used to continuously measure light attenuation on a particle-laden filter tape. AE33 measured 7 wavelengths of 370, 470, 520, 590, 660, 880 and 950 nm and MA200 measured 5 wavelengths of 375, 470, 528, 660 and 880 nm.

With aethalometers, absorption coefficients $b_{abs,AE}$ were calculated using

$$b_{abs,AE} = \frac{b_{atn,AE}}{C} = \frac{1}{C}\frac{A}{Q_{in}R}\frac{\Delta \mathrm{ATN}}{\Delta t}, \tag{6}$$

where $b_{atn,AE}$ is the attenuation coefficient; A the surface area of the filter tape spot; ΔATN the difference in light attenuation at the filter spot during Δt; Q_{in} the sample flow rate; R the shadowing correction, defined continuously with the onboard dual-spot correction algorithm for AE33[87] and MA200[88], and ATN the total attenuation at the sampled filter spot. The measured light attenuation was converted to light absorption using the multiple scattering coefficient C, defined as

$$C = \frac{b_{atn,AE}(880\ nm)}{b_{abs,PAX}(880\ nm)} \tag{7}$$

The absorption coefficient of PAX at 870 nm was converted to equivalent absorption at 880 nm with an assumed absorption Ångström exponent of 1. This assumption introduces negligible uncertainty given the similarity between the two wavelengths. The determined C, measured at 880 nm, was assumed constant over the measured wavelengths, as the wavelength dependence of C has been previously reported to be negligible[68]. Simultaneous measurement data from MA200 and PAX was not available, thus the MA200 C value was determined from C-adjusted AE33 measurements as good correlation between these two instruments has been demonstrated previously[88,89]. As Aethalometers are generally used for ambient measurements with relatively low BC concentrations, they were used here under highly diluted conditions using an extra ejector diluter. AE33 was operated at a flow rate of 2 l/min and MA200 at 0.10 l/min. The total dilution ratio for the Aethalometers was 1:1000.

Spectral dependence of light absorption by PM was depicted with the absorption Ångström exponent (AAE):

$$\mathrm{AAE}\left(\frac{\lambda_1}{\lambda_2}\right) = -\frac{\ln\left(\frac{\mathrm{b_{abs}}(\lambda_1)}{\mathrm{b_{abs}}(\lambda_2)}\right)}{\ln\left(\frac{\lambda_1}{\lambda_2}\right)}, \tag{8}$$

where λ_1 and λ_2 are two wavelengths of interest. AAE of BC is commonly assumed to be equal to 1, while uncoated BC has been shown to vary between AAE values of 0.7–1.1, and non-absorbing coatings can enhance AAE further up to 1.25[64]. For this reason, the BrC attribution determined by wavelength dependence in AE33 was validated using offline UV-vis analyses of methanol extractions from sampled filters.

Black carbon was measured in three different ways. Following the terminology recommended by Petzold et al. (2013), these measurements correspond to: (1) refractory BC (rBC) refers to mass determined by laser-induced incandescence, (2) elemental carbon (EC) to the thermal-optical carbon analysis method, and (3) equivalent BC (eBC) to mass derived from light absorbance.

Laser-induced incandescence was measured using a LII-300 (Artium Technologies Inc.), yielding an online retrieval of rBC concentrations. In the LII-300, sample aerosols are exposed to a nanosecond pulsed Nd:YAG laser (1064 nm). Particles that both absorb strongly at this wavelength and are refractory (i.e. rBC by definition) are heated to temperatures above 2500 K and incandesce. The intensity of this incandescence is proportional to the rBC mass concentration. The LII-300 uses the auto compensation technique, making use of the sample temperature measured using two-color pyrometry and the $\mathrm{MAC_{BC}}$[90–92]. Prior to the campaign, the rBC mass measurement was calibrated against thermal-optical EC produced by an aircraft turbine engine. The laser fluence of LII was set to 0.23 mJ/mm^2, near the transition between the low and high fluence regimes to avoid artifacts in the low fluence regime and sublimation at higher fluences. A flow rate of 0.5 l/min and a total dilution ratio of 1:100 was used for sampling.

Thermal-optical carbon analysis (TOA) with an offline OC/EC analyzer (Model 5 L, Sunset Laboratory, Inc.) was conducted to determine the elemental carbon (EC) content from quartz filters, which were collected during the campaign (See *Methods – Experimental* setup). In TOA, organic carbon is first volatilized in the presence of an inert gas, whilst incrementally increasing the temperature of the filter sample in steps. At sufficiently high temperatures, OC is expected to have been desorbed from the filter. After removing the OC fraction, the carrier gas is switched from inert gas to an oxygen-containing mixture. Hereafter EC is combusted from the filter, while the temperature is further raised in steps[93]. In the Sunset OC/EC analyzer, thermally desorbed carbon in the carrier gas is catalytically converted to methane and continuously measured with an FID during the heating procedure. Commonly a fraction of the OC becomes charred — referred to as pyrolytically converted carbon (PC) — during the inert heating phases, after which it does not readily desorb from the filter and is only combusted in the oxygen-containing phases. The darkening can be measured with transmittance/reflectance, seen as a drop in both transmittance and reflectance signals. In the first part of EC determination, while the sample is being combusted, the laser transmittance signal increases up to its baseline value. The "EC" measured up to this split point is defined as PC and assigned to OC, and the remaining carbon is attributed to original EC mass collected onto the filter[93].

Equivalent BC mass concentrations (c_{eBC}) from the light absorption measurements were determined using a mass absorption cross section of black carbon ($\mathrm{MAC_{BC}}$):

$$c_{eBC} = \frac{b_{abs}(\lambda_{NIR})}{\mathrm{MAC}_{BC}(\lambda_{NIR})} \tag{9}$$

where λ_{NIR} is a near-infrared wavelength (NIR). Wavelengths of 870 nm (PAX) and 880 nm (AE33, MA200) were used to derive eBC concentrations, based on the assumption that IR absorption is entirely caused by BC. However, in the context of marine emissions, this assumption may not always hold, as residual fuels have been reported to emit infrared-absorbing tar BrC[18], which may lead to overestimation of eBC. In $\mathrm{MAC_{BC}}$ determination, light absorption measurement from PAX was used, as it is devoid of filter tape artifacts, as noted above. The reference rBC was determined from LII instead of EC from the thermal-optical method, as LII and PAX were co-located with shared sampling lines; thus the effects of sampling line losses or filter sample handling and storage were avoided.

$$\mathrm{MAC}_{BC}(\lambda) = \frac{b_{abs,BC}(\lambda)}{c_{rBC}} \tag{10}$$

The baseline $\mathrm{MAC_{BC}}$ was calculated from fresh emissions at ≥75% engine loads, where the particle mass comprised mostly rBC, resulting in $\mathrm{MAC_{BC}}$ (870 nm) = 5.42 m^2/g and $\mathrm{MAC_{BC}}$ (880 nm) = 5.36 m^2/g. These represent $\mathrm{MAC_{BC}}$ values for minimally coated black carbon, which were also used for eBC conversion and increased values of $\mathrm{MAC_{BC}}$ were taken to indicate absorption enhancement ($E_{abs} = \mathrm{MAC}_{BC,coated}/\mathrm{MAC}_{BC,uncoated}$).

Aerosol chemical composition and size distributions

The chemical composition of non-refractory particulate matter was measured online with a HR-ToF-AMS (Aerodyne Inc.). In the AMS, non-refractory particulate matter (nrPM) with an aerodynamic diameter between 50 and 600 nm is transmitted through the aerodynamic lens and then flash vaporized by a heated ceramic furnace (600 °C). ToF-AMS Analysis Toolkit 1.65 (SQUIRREL) was used to process the AMS data. The high-resolution analyses were conducted using ToF-AMS HR Analysis 1.25 (PIKA). Further, elemental ratios, i.e. O/C, H/C, OC/OM ratios, were defined based on the Aiken method[94]. AMS was operated at a 1-minute time resolution, while total dilution ratios of 1:1000 for fresh emissions and 1:3000 for aged emissions were used, as the aged measurements included an extra 1:3 dilution.

A Single-Particle Mass Spectrometer (SP-MS; prototype of the PhotonLIZA system, Photonion GmbH, Germany) was used to characterize both refractory and non-refractory particle components at the single-particle level. The instrument's operating principle and parameters have been described in previous work[95]. In brief, particles with diameters above roughly 150 nm are detected and sized by light scattering, then sequentially exposed to laser pulses that desorb and ionize both inorganic and organic material. This provides information on inorganic species (metals, soot, salts) combined with molecular fingerprints of small molecules and non-polar aromatics[96,97]. In this study, we focus on ions generated by laser desorption/ionization (LDI) using 5 mJ UV pulses from a KrF excimer laser (248 nm). Part of the data was acquired in free-running mode, where optical detection was disabled and the ionization laser fired at 100 Hz without synchronization to the particle beam. This approach bypasses the lower size limit of the optical detection system and allows the analysis of particles as small as 50 nm. While SP-MS does not provide absolute mass concentrations on a per-particle basis, it yields characteristic chemical signatures, their temporal and compositional variability, and information on particle mixing state[98]. The SP-MS was operated under DR = 1:100.

Two scanning Mobility Particle Sizers (SMPS 3938, TSI Inc.) were deployed to measure the electrical mobility size distributions of fresh and aged particle emissions. Both SMPS instruments were operated on a 90 s loop (60 s scan followed by 4 s retrace, 10 s purge and 16 s wait). The combined dilution ratio for SMPS was DR = 1:1000.

Emission factor calculation

Emission factors (EF) are presented as the mass of a species emitted per kWh produced by the engine. EFs were calculated using:

$$\mathrm{EF} = \frac{c_m * Q_{ex}}{P_{out}}, \tag{11}$$

where EF is the emission factor (mg/kWh produced), c_m the mass concentration of a species (mg/m^3), Q_{ex} the exhaust volume flow rate (m^3/h) and P_{out} the power output of the engine (kW). Emission factors are primarily reported as mg/kWh, however, the conversion factors (m^3/kg$_{fuel}$) to derive EF as mass per consumed fuel (mg/kg$_{fuel}$) were also included in the supplement.

Statistical methods

Aerosol optical properties (AOP, i.e. MAC$_{BC}$, SSA, AAE, C) were analyzed using a linear mixed-effects model. The analysis was restricted to specified engine loads. Photochemical aging (fresh vs. aged) was included as a fixed effect, while fuel was treated as a random effect with a random intercept to account for between-fuel differences in baseline outcome. Temporal autocorrelation in the residuals arising from the time-series structure of the measurements was modeled using a first-order autoregressive [AR(1)] correlation structure based on the observation order within each fuel. The model can be summarized as:

$$AOP_{i,t} = \beta_0 + \beta_1 aged_{i,t} + b_{0,i} + \varepsilon_{i,t}, \tag{12}$$

$$b_{0,i} \sim \mathcal{N}\left(0, \sigma_b^2\right), \tag{13}$$

$$\varepsilon_{i,t} = \phi \varepsilon_{i,t-1} + \eta_{i,t}, \tag{14}$$

and

$$\eta_{i,t} \sim \mathcal{N}\left(0, \sigma^2\right), \tag{15}$$

where i indexes fuel type and t indexes time, β_0 is the fixed intercept, β_1 represents the fixed effect of aerosol ageing (fresh vs. aged), $b_{0,i}$ and is a fuel-specific random intercept capturing between-fuel differences in baseline AOP. The residuals $\varepsilon_{i,t}$ follow a first-order autoregressive [AR(1)] process with an autocorrelation parameter ϕ, accounting for temporal dependence between consecutive observations within each fuel.

Data availability

The main data is available in the online repository DOI:10.5281/zenodo.17344025. Particle mobility size distribution data from the same experiments has been published in Shukla et al. (2025), DOI:10.1039/d5ea00040h. Additional datasets associated with the study are available from the corresponding authors on reasonable request.

Received: 15 October 2025; Accepted: 24 February 2026;

References

1. The Marine Environment Protection Committee (MEPC). Resolution MEPC.192 (61). 2010 guidelines for monitoring the worldwide average sulphur content of fuel oils supplied for use on board ships. (2010).
2. Corbett, J. J. et al. Health Impacts Associated with Delay of MARPOL Global Sulphur Standards. (2016).
3. The Marine Environment Protection Committee (MEPC). Resolution MEPC.329(76). Amendments to the annex of the international convention for the prevention of pollution from ships, 1973, as modified by the protocol of 1978 relating thereto. (2021).
4. Comer, B., Osipova, L., Georgeff, E. & Mao, X. The international maritime organization's proposed arctic heavy fuel oil ban: Likely impacts and opportunities for improvement. *Int. Counc. Clean Transp*. https://theicct.org/wp-content/uploads/2021/06/Arctic-HFO-ban-sept2020.pdf (2020).
5. Screen, J. A. & Simmonds, I. The central role of diminishing sea ice in recent Arctic temperature amplification. *Nature* **464**, 1334–1337 (2010).
6. Rantanen, M. et al. The Arctic has warmed nearly four times faster than the globe since 1979. *Commun. Earth Environ.* **3**, 168 (2022).
7. Walsh, J. E., Fetterer, F., Scott Stewart, J. & Chapman, W. L. A database for depicting Arctic sea ice variations back to 1850. *Geogr. Rev.* **107**, 89–107 (2017).
8. Laakso, L. et al. 100 years of atmospheric and marine observations at the Finnish Utö Island in the Baltic Sea. *Ocean Sci.* **14**, 617–632 (2018).
9. Messner, S. Future Arctic shipping, black carbon emissions, and climate change. in *Maritime Transport and Regional Sustainability* 195–208 (Elsevier, 2020).
10. PAME. The Increase In Arctic Shipping 2013–2019. *Arct. Shipp. Status Rep. 1* (2024).
11. Diamond, M. S., Director, H. M., Eastman, R., Possner, A. & Wood, R. Substantial cloud brightening from shipping in subtropical low clouds. *AGU Adv.* **1**, e2019AV000111 (2020).
12. Watson-Parris, D. et al. Surface temperature effects of recent reductions in shipping SO_2 emissions are within internal variability. *Atmos. Chem. Phys.* **25**, 4443–4454 (2025).
13. Yoshioka, M., Grosvenor, D. P., Booth, B. B. B., Morice, C. P. & Carslaw, K. S. Warming effects of reduced sulfur emissions from shipping. *Atmos. Chem. Phys.* **24**, 13681–13692 (2024).
14. Gettelman, A. et al. Has reducing ship emissions brought forward global warming? *Geophys. Res. Lett.* **51**, e2024GL109077 (2024).

15. Diamond, M. S. Detection of large-scale cloud microphysical changes within a major shipping corridor after implementation of the International Maritime Organization 2020 fuel sulfur regulations. *Atmos. Chem. Phys.* **23**, 8259–8269 (2023).
16. Yuan, T. et al. Global reduction in ship-tracks from sulfur regulations for shipping fuel. *Sci. Adv.* **8**, eabn7988 (2022).
17. Partanen, A. I. et al. Climate and air quality trade-offs in altering ship fuel sulfur content. *Atmos. Chem. Phys.* **13**, 12059–12071 (2013).
18. Corbin, J. C. et al. Infrared-absorbing carbonaceous tar can dominate light absorption by marine-engine exhaust. *Npj Clim. Atmos. Sci.* **2**, 12 (2019).
19. Corbin, J. C. et al. Brown and black carbon emitted by a marine engine operated on heavy fuel oil and distillate fuels: Optical properties, size distributions, and emission factors. *J. Geophys. Res. Atmos.* **123**, 6175–6195 (2018).
20. Ødemark, K. et al. Short-lived climate forcers from current shipping and petroleum activities in the Arctic. *Atmos. Chem. Phys.* **12**, 1979–1993 (2012).
21. Bond, T. C. et al. Bounding the role of black carbon in the climate system: A scientific assessment. *J. Geophys. Res. Atmos.* **118**, 5380–5552 (2013).
22. Corbin, J. C. et al. Characterization of particulate matter emitted by a marine engine operated with liquefied natural gas and diesel fuels. *Atmos. Environ.* **220**, 117030 (2020).
23. Helin, A. et al. Variation of absorption ångström exponent in aerosols from different emission sources. *J. Geophys. Res. Atmos.* **126**, e2020JD034094 (2021).
24. Streibel, T. et al. Aerosol emissions of a ship diesel engine operated with diesel fuel or heavy fuel oil. *Environ. Sci. Pollut. Res.* **24**, 10976–10991 (2017).
25. Lack, D. A. et al. Particulate emissions from commercial shipping: Chemical, physical, and optical properties. *J. Geophys. Res. Atmos.* **114**, 2008JD011300 (2009).
26. Sun, C. et al. Morphological and optical properties of carbonaceous aerosol particles from ship emissions and biomass burning during a summer cruise measurement in the South China Sea. *Atmos. Chem. Phys.* **24**, 3043–3063 (2024).
27. Corbin, J. C. & Gysel-Beer, M. Detection of tar brown carbon with a single particle soot photometer (SP2). *Atmos. Chem. Phys.* **19**, 15673–15690 (2019).
28. Cappa, C. D. et al. Radiative Absorption Enhancements Due to the Mixing State of Atmospheric Black Carbon. *Science* **337**, 1078–1081 (2012).
29. Fierce, L. et al. Radiative absorption enhancements by black carbon controlled by particle-to-particle heterogeneity in composition. *Proc. Natl. Acad. Sci.* **117**, 5196–5203 (2020).
30. Fu, X. et al. Evolution of light absorption enhancement of black carbon aerosols from biomass burning in atmospheric photochemical aging. *J. Geophys. Res. Atmos.* **129**, e2024JD040756 (2024).
31. Corbin, J. C., Modini, R. L. & Gysel-Beer, M. Mechanisms of soot-aggregate restructuring and compaction. *Aerosol Sci. Technol.* **57**, 89–111 (2023).
32. Miljevic, B., Surawski, N. C., Bostrom, T. & Ristovski, Z. D. Restructuring of carbonaceous particles upon exposure to organic and water vapours. *J. Aerosol Sci.* **47**, 48–57 (2012).
33. Radney, J. G. et al. Dependence of soot optical properties on particle morphology: Measurements and model comparisons. *Environ. Sci. Technol.* **48**, 3169–3176 (2014).
34. Kumar, N. K. et al. Production of particulate brown carbon during atmospheric aging of residential wood-burning emissions. *Atmos. Chem. Phys.* **18**, 17843–17861 (2018).
35. Laskin, A., Laskin, J. & Nizkorodov, S. A. Chemistry of atmospheric brown carbon. *Chem. Rev.* **115**, 4335–4382 (2015).
36. Adachi, K. et al. Spherical tarball particles form through rapid chemical and physical changes of organic matter in biomass-burning smoke. *Proc. Natl. Acad. Sci.* **116**, 19336–19341 (2019).
37. Friebel, F. et al. Impact of isolated atmospheric aging processes on the cloud condensation nuclei activation of soot particles. *Atmos. Chem. Phys.* **19**, 15545–15567 (2019).
38. Zhang, R. et al. Variability in morphology, hygroscopicity, and optical properties of soot aerosols during atmospheric processing. *Proc. Natl. Acad. Sci.* **105**, 10291–10296 (2008).
39. Henning, S. et al. Hygroscopic growth and droplet activation of soot particles: uncoated, succinic or sulfuric acid coated. *Atmos. Chem. Phys.* **12**, 4525–4537 (2012).
40. Leskinen, J. et al. Photochemical aging induces changes in the effective densities, morphologies, and optical properties of combustion aerosol particles. *Environ. Sci. Technol.* **57**, 5137–5148 (2023).
41. Zhang, Y. et al. Evidence of major secondary organic aerosol contribution to lensing effect black carbon absorption enhancement. *Npj Clim. Atmos. Sci.* **1**, 47 (2018).
42. Hartikainen, A. H. et al. Photochemical transformation and secondary aerosol formation potential of Euro6 gasoline and diesel passenger car exhaust emissions. *J. Aerosol Sci.* **171**, 106159 (2023).
43. Hartikainen, A. et al. Photochemical aging of aviation emissions: transformation of chemical and physical properties of exhaust emissions from a laboratory-scale jet engine combustion chamber. *Atmos. Chem. Phys.* **25**, 9275–9294 (2025).
44. Lack, D. A. & Cappa, C. D. Impact of brown and clear carbon on light absorption enhancement, single scatter albedo and absorption wavelength dependence of black carbon. *Atmos. Chem. Phys.* **10**, 4207–4220 (2010).
45. Popovicheva, O. et al. Ship particulate pollutants: Characterization in terms of environmental implication. *J. Environ. Monit.* **11**, 2077 (2009).
46. Popovicheva, O. et al. Microscopic characterization of individual particles from multicomponent ship exhaust. *J. Environ. Monit.* **14**, 3101 (2012).
47. Moldanová, J. et al. Characterisation of particulate matter and gaseous emissions from a large ship diesel engine. *Atmos. Environ.* **43**, 2632–2641 (2009).
48. Suzuki, S. & Mori, S. Carbon nanotube-like materials in the exhaust from a diesel engine using gas oil/ethanol mixing fuel with catalysts and sulfur. *J. Air Waste Manag. Assoc.* **67**, 873–880 (2017).
49. Jung, H. S., Miller, A., Park, K. & Kittelson, D. B. Carbon nanotubes among diesel exhaust particles: real samples or contaminants?. *J. Air Waste Manag. Assoc.* **63**, 1199–1204 (2013).
50. Aakko-Saksa, P. et al. Suitability of different methods for measuring black carbon emissions from marine engines. *Atmosphere* **13**, 31 (2021).
51. Liu, F. et al. Review of recent literature on the light absorption properties of black carbon: Refractive index, mass absorption cross section, and absorption function. *Aerosol Sci. Technol.* **54**, 33–51 (2020).
52. Bond, T. C. & Bergstrom, R. W. Light Absorption by Carbonaceous Particles: An Investigative Review. *Aerosol Sci. Technol.* **40**, 27–67 (2006).
53. Chakrabarty, R. K. & Heinson, W. R. Scaling laws for light absorption enhancement due to nonrefractory coating of atmospheric black carbon aerosol. *Phys. Rev. Lett.* **121**, 218701 (2018).
54. McMeeking, G. R. et al. Impacts of nonrefractory material on light absorption by aerosols emitted from biomass burning. *J. Geophys. Res. Atmospheres.* **119**, 12272–12286 (2014).
55. Yus-Díez, J. et al. Absorption enhancement of black carbon particles in a Mediterranean city and countryside: effect of particulate matter chemistry, ageing and trend analysis. *Atmos. Chem. Phys.* **22**, 8439–8456 (2022).
56. He, C. et al. Variation of the radiative properties during black carbon aging: theoretical and experimental intercomparison. *Atmos. Chem. Phys.* **15**, 11967–11980 (2015).

57. Zhang, X., Mao, M., Yin, Y. & Wang, B. Numerical investigation on absorption enhancement of black carbon aerosols partially coated with nonabsorbing organics. *J. Geophys. Res. Atmos.* **123**, 1297–1308 (2018).
58. Moise, T., Flores, J. M. & Rudich, Y. Optical properties of secondary organic aerosols and their changes by chemical processes. *Chem. Rev.* **115**, 4400–4439 (2015).
59. Eichler, P. et al. Lubricating oil as a major constituent of ship exhaust particles. *Environ. Sci. Technol. Lett.* **4**, 54–58 (2017).
60. Lesins, G., Chylek, P. & Lohmann, U. A study of internal and external mixing scenarios and its effect on aerosol optical properties and direct radiative forcing. *J. Geophys. Res. Atmos.* **107**, D10 (2002).
61. Elser, M. et al. Chemical composition and radiative properties of nascent particulate matter emitted by an aircraft turbofan burning conventional and alternative fuels. *Atmos. Chem. Phys.* **19**, 6809–6820 (2019).
62. Chen, Y. & Bond, T. C. Light absorption by organic carbon from wood combustion. *Atmos. Chem. Phys.* **10**, 1773–1787 (2010).
63. Chýlek, P., Videen, G., Ngo, D., Pinnick, R. G. & Klett, J. D. Effect of black carbon on the optical properties and climate forcing of sulfate aerosols. *J. Geophys. Res. Atmos.* **100**, 16325–16332 (1995).
64. Luo, J., Zhang, Y. & Zhang, Q. The ångström exponent and single-scattering albedo of black carbon: Effects of different coating materials. *Atmosphere* **11**, 1103 (2020).
65. Virkkula, A. Modeled source apportionment of black carbon particles coated with a light-scattering shell. *Atmos. Meas. Tech.* **14**, 3707–3719 (2021).
66. Backman, J. et al. On Aethalometer measurement uncertainties and an instrument correction factor for the Arctic. *Atmos. Meas. Tech.* **10**, 5039–5062 (2017).
67. Bernardoni, V. et al. Determination of Aethalometer multiple-scattering enhancement parameters and impact on source apportionment during the winter 2017/18 EMEP/ACTRIS/COLOSSAL campaign in Milan. *Atmos. Meas. Tech.* **14**, 2919–2940 (2021).
68. Yus-Díez, J. et al. Determination of the multiple-scattering correction factor and its cross-sensitivity to scattering and wavelength dependence for different AE33 Aethalometer filter tapes: a multi-instrumental approach. *Atmos. Meas. Tech.* **14**, 6335–6355 (2021).
69. Zhang, Y. et al. Developing a dynamic correction mechanism for aethalometer results of actual urban aerosols. *Atmos. Res* **255**, 105529 (2021).
70. Bauer, M. et al. Impact of fuel sulfur regulations on carbonaceous particle emission from a marine engine. *Npj Clim. Atmos. Sci.* **7**, 288 (2024).
71. Lauer, P., Behrends, D. B., Ltd, M., Hinz, M. & Eylmann, S. Luftschadstoffe in der Seeschifffahrt – Erstellung einer Maßnahmenmatrix der Minderungsoptionen sowie Durchführung und Analyse einer Black Carbon-Messkampagne in Abhängigkeit von der Kraftstoffqualität. *Umw. Bundesamt* (2024).
72. Karjalainen, P. et al. Real-world particle emissions and secondary aerosol formation from a diesel oxidation catalyst and scrubber equipped ship operating with two fuels in a SECA area. *Environ. Pollut.* **292**, 118278 (2022).
73. Bambha, R. P., Dansson, M. A., Schrader, P. E. & Michelsen, H. A. Effects of volatile coatings on the laser-induced incandescence of soot. *Appl. Phys. B* **112**, 343–358 (2013).
74. Aakko-Saksa, P. et al. Considerations in analysing elemental carbon from marine engine exhaust using residual, distillate and biofuels. *J. Aerosol Sci.* **126**, 191–204 (2018).
75. Lappi, M. K. & Ristimäki, J. M. Evaluation of thermal optical analysis method of elemental carbon for marine fuel exhaust. *J. Air Waste Manag. Assoc.* **67**, 1298–1318 (2017).
76. Sipkens, T. A. et al. Quantifying the uncertainties in thermal–optical analysis of carbonaceous aircraft engine emissions: an interlaboratory study. *Atmos. Meas. Tech.* **17**, 4291–4302 (2024).
77. Aakko-Saksa, P. T. et al. Reduction in greenhouse gas and other emissions from ship engines: Current trends and future options. *Prog. Energy Combust. Sci.* **94**, 101055 (2023).
78. Sippula, O. et al. Particle Emissions from a Marine Engine: Chemical Composition and Aromatic Emission Profiles under Various Operating Conditions. *Environ. Sci. Technol.* **48**, 11721–11729 (2014).
79. Mueller, L. et al. Characteristics and temporal evolution of particulate emissions from a ship diesel engine. *Appl. Energy* **155**, 204–217 (2015).
80. Paul, A. et al. The impact of photochemical aging on secondary aerosol formation from a marine engine. *Npj Clim. Atmos. Sci.* **8**, 106 (2025).
81. Shukla, D. et al. Emission speciation of volatile and intermediate volatility organic compounds from a marine engine: effect of engine load, fuel type and photochemical aging. *Environ. Sci. Atmos.* **5**, 973–986 (2025).
82. Ihalainen, M. et al. A novel high-volume photochemical emission aging flow tube reactor (PEAR). *Aerosol Sci. Technol.* **53**, 276–294 (2019).
83. Sipkens, T. A. & Rogak, S. N. Technical note: Using k-means to identify soot aggregates in transmission electron microscopy images. *J. Aerosol Sci.* **152**, 105699 (2021).
84. Barmet, P. et al. OH clock determination by proton transfer reaction mass spectrometry at an environmental chamber. *Atmos. Meas. Tech.* **5**, 647–656 (2012).
85. Moosmüller, H., Chakrabarty, R. K. & Arnott, W. P. Aerosol light absorption and its measurement: A review. *J. Quant. Spectrosc. Radiat. Transf.* **110**, 844–878 (2009).
86. Peñaloza, M. A. Deriving the basic cell-reciprocal integrating nephelometer equation and its use for calibration purposes: a comprehensive approach. *Meas. Sci. Technol.* **10**, R1–R15 (1999).
87. Drinovec, L. et al. The 'dual-spot' Aethalometer: an improved measurement of aerosol black carbon with real-time loading compensation. *Atmos. Meas. Tech.* **8**, 1965–1979 (2015).
88. Chakraborty, M., Giang, A. & Zimmerman, N. Performance evaluation of portable dual-spot micro-aethalometers for source identification of black carbon aerosols: application to wildfire smoke and traffic emissions in the Pacific Northwest. *Atmos. Meas. Tech.* **16**, 2333–2352 (2023).
89. Cai, J. et al. Validation of MicroAeth® as a Black Carbon Monitor for Fixed-Site Measurement and Optimization for Personal Exposure Characterization. *Aerosol Air Qual. Res.* **14**, 1–9 (2014).
90. De Iuliis, S., Cignoli, F. & Zizak, G. Two-color laser-induced incandescence (2C-LII) technique for absolute soot volume fraction measurements in flames. *Appl. Opt.* **44**, 7414 (2005).
91. Mehri, R., Sipkens, T. A., Smallwood, G. J., Johnson, M. & Corbin, J. C. Size-resolved measurements of the light absorption properties of soot aerosols from a gas turbine engine. *Appl. Phys. B* **131**, 98 (2025).
92. Snelling, D. R., Smallwood, G. J., Liu, F., Gülder, ÖL. & Bachalo, W. D. A calibration-independent laser-induced incandescence technique for soot measurement by detecting absolute light intensity. *Appl. Opt.* **44**, 6773 (2005).
93. Chow, J. C. et al. The IMPROVE_A temperature protocol for thermal/optical carbon analysis: Maintaining consistency with a long-term database. *J. Air Waste Manag. Assoc.* **57**, 1014–1023 (2007).
94. Aiken, A. C., DeCarlo, P. F. & Jimenez, J. L. Elemental analysis of organic species with electron ionization high-resolution mass spectrometry. *Anal. Chem.* **79**, 8350–8358 (2007).
95. Schade, J. et al. Spatially shaped laser pulses for the simultaneous detection of polycyclic aromatic hydrocarbons as well as positive and negative inorganic ions in single particle mass spectrometry. *Anal. Chem.* **91**, 10282–10288 (2019).
96. Anders, L. et al. Detection of ship emissions from distillate fuel operation *via* single-particle profiling of polycyclic aromatic hydrocarbons. *Environ. Sci. Atmos.* **3**, 1134–1144 (2023).

97. Schmidt, M. et al. A solid-state infrared laser for two-step desorption–ionization processes in single-particle mass spectrometry. *Atmos. Meas. Tech.* **18**, 2425–2437 (2025).
98. Passig, J. & Zimmerman, R. Laser Ionization in Single-Particle Mass Spectrometry. in R. Zimmermann&L. Hanley (Eds.), Photoionization and Photo-Induced Processes in Mass Spectrometry 359-411 (Wiley-VCH, Weinheim, Deutschland, 2021).

Acknowledgements

This work was funded by the European Union Horizon 2020 project ULTRHAS (project number 955390), Deutsche Forschungsgemeinschaft (DFG, German Research Foundation)—SFB 1477 "Light-Matter Interactions at Interfaces" (project number 441234705), and Research Council of Finland "Black and Brown Carbon in the Atmosphere and the Cryosphere" (BBrCAC) (project number 341597) and "Competitive funding to strengthen university research profiles [PROFI] for the University of Eastern Finland" (project number 352968). Additional funding was provided by Transport Canada. Views and opinions expressed are those of the authors only and do not necessarily reflect those of the European Union. Neither the European Union nor the granting authority can be held responsible for them.

Author contributions

T.K., A.P., D.S., M.I., A.D., J.S., J.P., A.K., U.E., Z.F. and M.S. carried out the measurements. A.P. processed the data of the HR-ToF-AMS. J.P. processed the data of the SP-MS. T.K. processed the data of other online instruments. T.A.S. conducted the electron microscopy analyses. T.K., V.L. and A.M. performed the OC/EC and UV-vis analyses. T.K. and T.A.S. prepared the graphical figures. H.C., B.B., T.S., T.H., Y.R., J.Ø., R.Z., J.C.C. and O.S. acquired funding and supervised the work. T.K. wrote the main manuscript with inputs from T.A.S., A.P., D.S., M.I., J.P., S.M., A.H., J.C.C. and O.S. T.A.S., A.P., D.S., M.I., J.P., S.M., A.H., H.C., T.S., T.H., Y.R., R.Z., J.C.C. and O.S. reviewed the manuscript.

Competing interests

The authors declare no competing interests.

Additional information

Supplementary information The online version contains supplementary material available at https://doi.org/10.1038/s41612-026-01369-w.

Correspondence and requests for materials should be addressed to Tuukka Kokkola or Olli Sippula.

Reprints and permissions information is available at http://www.nature.com/reprints